JOURNAL OF GEOPHYSICAL RESEARCH, VOL. 105, NO. B2, PAGES 2699-2719, FEBRUARY 10, 2000

Crustal and upper mantle seismic structure beneath the rift mountains and across a nontransform offset at the Mid-Atlantic Ridge (35°N)

J. Pablo Canales, Robert S. Detrick, Jian Lin, and John A. Collins
Department of Geology and Geophysics, Woods Hole Oceanographic Institution, Woods Hole, Massachusetts

Douglas R. Toomey
Department of Geologocal Sciences, University of Oregon, Eugene, Oregon

Abstract. We present new results on the crustal and upper mantle structure beneath the rift mountains along two segments of the Mid-Atlantic Ridge and across a nontransform offset (NTO). Our results were obtained from a combination of forward modeling and two-dimensional tomographic inversion of wide-angle seismic refraction data and gravity modeling. The study area includes two segments: OH-1 between the Oceanographer fracture zone and the NTO-1 at 34°35'N and OH-2 between NTO-1 and the NTO at 34°10'N. The center of OH-1 is characterized by anomalously thick crust (~8 km) with a thick Moho transition zone with V_p=7.2-7.6 km/s. This transition zone, coincident with a gravity low, is probably composed of gabbro sills alternating with dunites, as observed in some ophiolites. OH-1 has larger along-axis crustal thickness variations than OH-2, but average crustal thicknesses are similar (6.0±1.2 km at OH-1, 6.1±0.7 at OH-2). Thus we do not find significant differences in magma supply between these segments, in contrast to what has been inferred from morphological and gravity studies. At both segments the shoaling of the Moho is more rapid at the inside than at the outside corners, consistent with models in which the inside-corner crust is tectonically modified. The structural differences between inside- and outside-corner crust are more apparent at OH-2, suggesting that the extrusive layer is thinner at the inside corner of OH-2 than at the inside corner of OH-1, probably due to differences in axial morphology and along-axis magma transport. NTO-1 is characterized by a nearly constant velocity gradient within the upper 5 km and low upper mantle velocities (7.4-7.8 km/s). The anomalous structure beneath NTO-1 is interpreted as fractured mafic crust. The *P* wave velocities and densities required to match the gravity data suggest that serpentinites are common beneath the NTO-1 and possibly beneath the inside corners. Serpentinization could be as much as 40% at ~3.8 km below seafloor and probably does not occur at subseafloor depths greater than ~6.2 km at the NTO-1. Our results indicate that in a slow spreading environment where magmatism and tectonism are equally important, the seismic Moho cannot be correlated with an unique geological structure. At the center of a segment the seismic Moho may represent the lower boundary of an interlayered grabbro-dunite transition zone, while beneath the inside corner and NTO where the crust is thinner, it may correspond to an alteration front.

1. Introduction

Slow spreading ridges, like the Mid-Atlantic Ridge (MAR), are formed by a series of spreading segments, 20-100 km in length [*Schouten et al.*, 1985], separated by both transform and nontransform offsets (NTO). Typically, each segment is characterized by an axial valley where volcanism occurs and new crust is generated, flanked by elevated rift mountains. The depth and width of the rift valley vary considerably among segments, ranging between 1.0-2.8 km and 15-30 km, respectively [*Macdonald*, 1986]. Within a segment bounded by offsets of similar sense, three distinct tectonic and volcanic corridors are distinguished (Figure 1) [e.g., *Tucholke and Lin,* 1994]: inside corner, which is the section of the segment that abuts the active portion of a discontinuity; outside corner, on the opposite side of the segment and bounded by the inactive trace of a discontinuity; and segment center, the section between the inside and outside corners.

These areas have distinct characteristics probably due to focused magmatic accretion at the center of the segments [*Kuo and Forsyth*, 1988; *Lin et al.,* 1990] and tectonic alteration of the inside-corner crust along low-angle faults [*Dick et al*., 1981; *Karson and Dick*, 1983; *Tucholke and Lin*, 1994]: For topography, the seafloor progressively deepens along a segment, from the inside to the outside corner [*Severinghaus and Macdonald*, 1988]. For gravity, inside corners are associated with positive gravity anomalies [*Blackman and Forsyth*, 1991; *Escartín and Lin*, 1995], segment centers with prominent "bull's-eye" gravity lows [*Kuo and Forsyth*, 1988; *Lin et al.,* 1990], and outside corners have a gravity signature intermediate between inside corner and segment center. For lithology, exposures of lower crust and upper mantle rocks are

Paper number 1999JB900379
0148-0227/00/1999JB900379$09.00

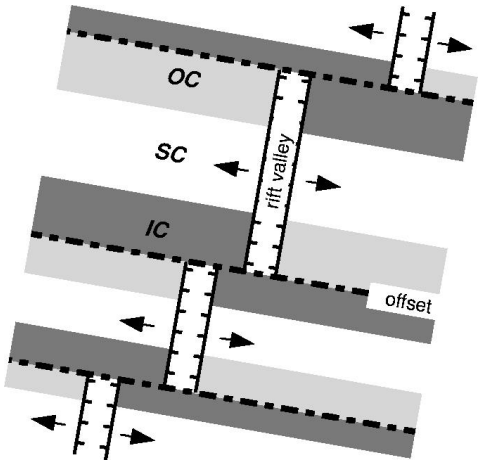

Figure 1. Schematic cartoon of two spreading segments bounded by offsets of similar sense. White areas are the center of the segments (SC), light shaded areas are outside corners (OC), and dark shaded areas are inside corners (IC). Arrows indicate spreading direction.

common at the inside corners [*Karson and Dick*, 1983; *Mével et al.,* 1991] but rare at the outside corners [*Tucholke and Lin*, 1994]. In contrast, basalts and diabases are more frequent at the outside corners and segment centers than at the inside corners [*Cannat et al*., 1995]. For morphology, the outside corner and segment center have hummocky volcanic morphology and volcanic cones, while the inside corner usually has few volcanic features [*Smith and Cann*, 1992]. More irregular, larger, and more widely spaced faults and abyssal hills are observed at inside than at outside corners and segment centers [*Shaw*, 1992; *Shaw and Lin*, 1993; *Goff et al*., 1995]. For magnetization, the inside-corner crust has higher induced magnetization than the outside-corner crust [*Tivey and Tucholke*, 1998].

Nontransform offsets are the most common discontinuities along the MAR [*Sempéré et al*., 1993]. The seismic structure at small NTOs resembles that observed at larger fracture zones [e.g., *Detrick et al*., 1993]. They exhibit thin crust and a nearly constant velocity gradient from extrusive basalts to ultramafic velocities, which results in the lack of ocean seismic layer 3. This has been attributed to a thin, highly fractured mafic crust, overlaying peridotites partially serpentinized due to hydrothermal alteration [*Detrick and Purdy*, 1980; *White et al*., 1984; *Minshull et al*., 1991]. The systematic crustal variability across NTOs has been confirmed by segment-scale gravity studies [*Kuo and Forsyth*, 1988; *Lin et al*., 1990; *Blackman and Forsyth*, 1991]. The active section of NTOs appears to be characterized by massifs where ultramafic rocks are exposed [*Gràcia et al*., 1997].

The pattern of along-isochron crustal and upper mantle variability at the MAR suggested by geological and geophysical data can be tested using combined modeling of seismic and gravity data. In this paper we present the results of a seismic experiment carried out along the rift mountains of two segments of the MAR near 35°N and across a nontransform offset. The goals of this study are to provide seismic constraints on the structure of the inside and outside corners and the center of two adjacent spreading segments, to analyze the nature of the Moho transition zone, especially where the bull's-eye gravity lows are observed, and to better understand the structure of an NTO. We will show that the center of a segment with a shallow axial valley is characterized by a thick Moho transition zone with anomalously high *P* wave velocities. We also find that the NTO has an anomalous crustal structure, probably due to crustal fractures and serpentinization of the upper mantle. Our results also suggest that the nature of the seismically defined Moho varies along-axis, from a lithological boundary to an alteration front.

2. Tectonic Setting

Our study area (Figure 2a) comprises two spreading segments of the MAR (named OH-1 and OH-2), and a nontransform offset that separates them (NTO-1). They are part of a group of five second-order segments bounded on the north by the Oceanographer fracture zone (OFZ) and on the south by the Hayes fracture zone [*Detrick et al*., 1995]. The half spreading rate in the area is 10-11 mm/yr [*LeDouaran et al*., 1982; *DeMets et al*., 1990]. OH-1 and OH-2 are the two northernmost segments and display different axial morphologies and gravity signatures.

OH-1 is a 90-km-long segment bounded on the north by the OFZ at 35°15'N and on the south by NTO-1 at 34°35'N (Figure 2b). The hourglass-shaped axial valley is shallow (2000 m) and narrow (4 km) at the midpoint and deeper (3300-4000 m) and wider (10-20 km) at its ends. Both flanks of the axis display the characteristic topographic asymmetry between inside and outside corner. This asymmetry is more pronounced in the eastern rift mountains where the inside corner bounds the active Oceanographer transform (water depth 890 m) than in the western rift mountains where the inside corner is bounded by NTO-1 (minimum water depth 1350 m). The center of OH-1 is intersected by a chain of volcanic cones trending parallel to the spreading direction and extending off-axis for at least 20 km. Submersible sampling and detailed magnetic measurements [*Bideau et al*., 1996] suggest that the volcanoes were probably formed on the axial valley floor. The inner valley is mostly covered by pillow lavas and sheet flows [*Bideau et al*., 1996], but no petrological information is available from the inside and outside corners of OH-1. Within the inner valley of OH-1 the upper crust has a thick transition from volcanic extrusives to intrusives, and it is strongly heterogeneous and anisotropic (2-4%) at depths shallower than 1.5 km due to cracks aligned parallel to the ridge axis [*Barclay et al*., 1998]. Beneath one of the volcanic cones, a low-velocity zone produced by high temperatures and possible partial melt is present. *Magde et al*. [1999] have mapped similar low velocities at shallow crustal levels along the rift valley of OH-1, while in the lower crust these low velocities are confined to the center of the segment. Segment OH-1 shows a large (40 mGal peak to trough) bull's-eye gravity low at its center and a distinct gravity asymmetry between the inside and outside corners [*Detrick et al*., 1995]. From a gravity analysis, *Detrick et al*. [1995] inferred that the crust is 8-9 km thick at the axial center of OH-1 and that the crustal thickness variation along the eastern flank may be 2-3 km from the inside to the outside corner. In contrast, the western flank shows very little difference in crustal thickness between the segment ends. The gravity-derived crustal thicknesses are in good agreement with that obtained by seismic methods at the center of the axial valley (line B in Figure 2b), where the crust is 8.2 km thick [*Hooft et al*., 1999], and along the eastern rift mountains (line D in Figure 2b), where it is 9-10

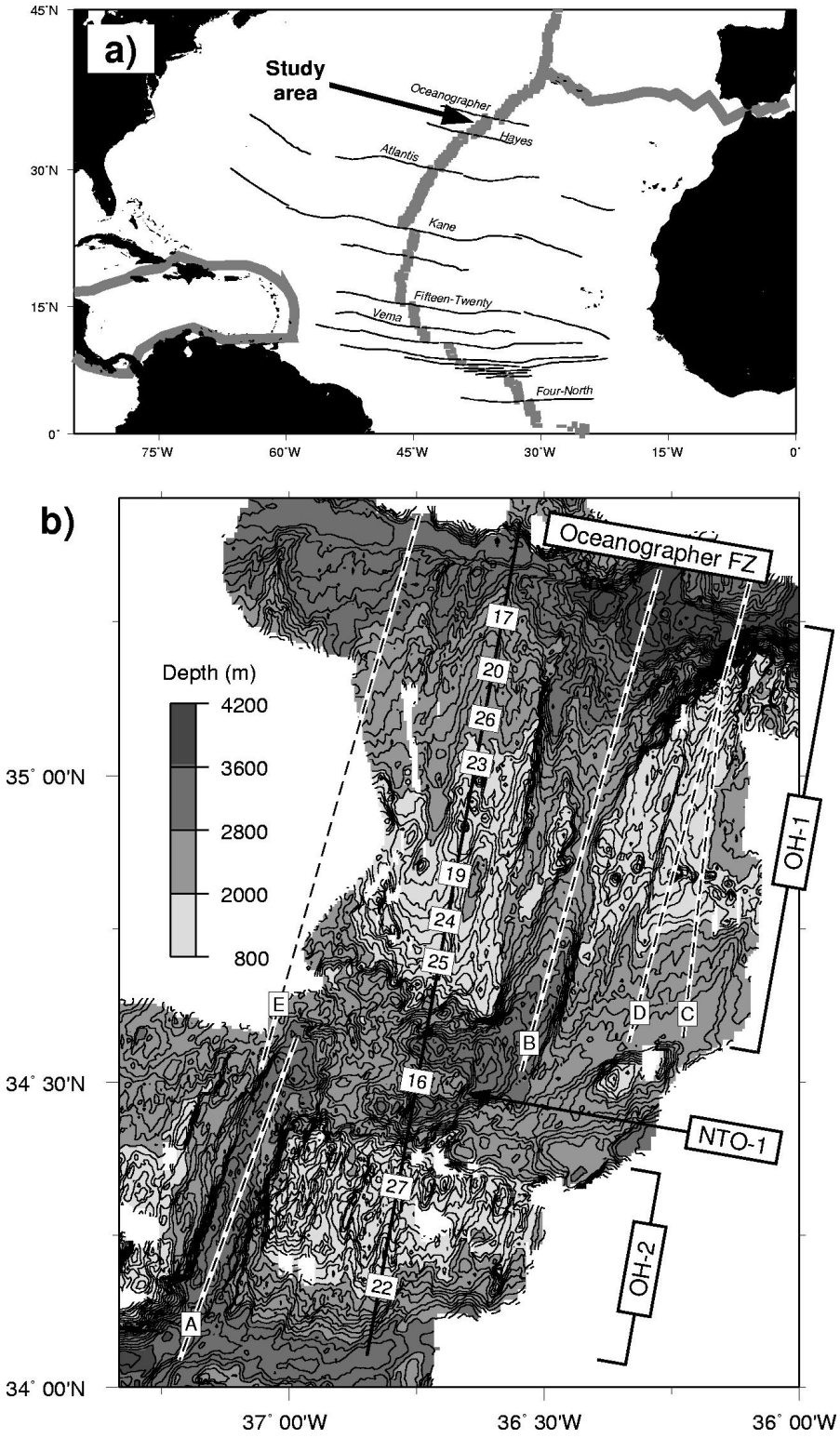

Figure 2. (a) Location of study area. Shaded bands are plate boundaries. Main central Atlantic fracture zones (solid lines) are labeled. (b) Bathymetry of the study area (Mid-Atlantic Ridge near 35°N). Spreading segments OH-1 and OH-2, the nontransform discontinuity (NTO-1), and the Oceanographer fracture zone are labeled. Note the differences in axial morphology between OH-1 (shallow axial valley that nearly disappears at 34°55'N, disrupted by volcanic cones) and OH-2 (deep and continuous axial valley) that suggest contrasting magmatic activity. Also, the topographic asymmetry between inside and outside corners is apparent at the rift mountains of both segments. Contours are every 100 m. Thick solid line is the seismic refraction profile MARBE3. Enclosed numbers indicate the location of the ocean bottom hydrophones. Dashed lines are other seismic refraction profiles in the area mentioned in the text: A and B are from *Hooft et al*. [1999], C is from *Hosford et al.* [1998], D and E are from *Sinha and Louden* [1983] and *White et al.* [1984].

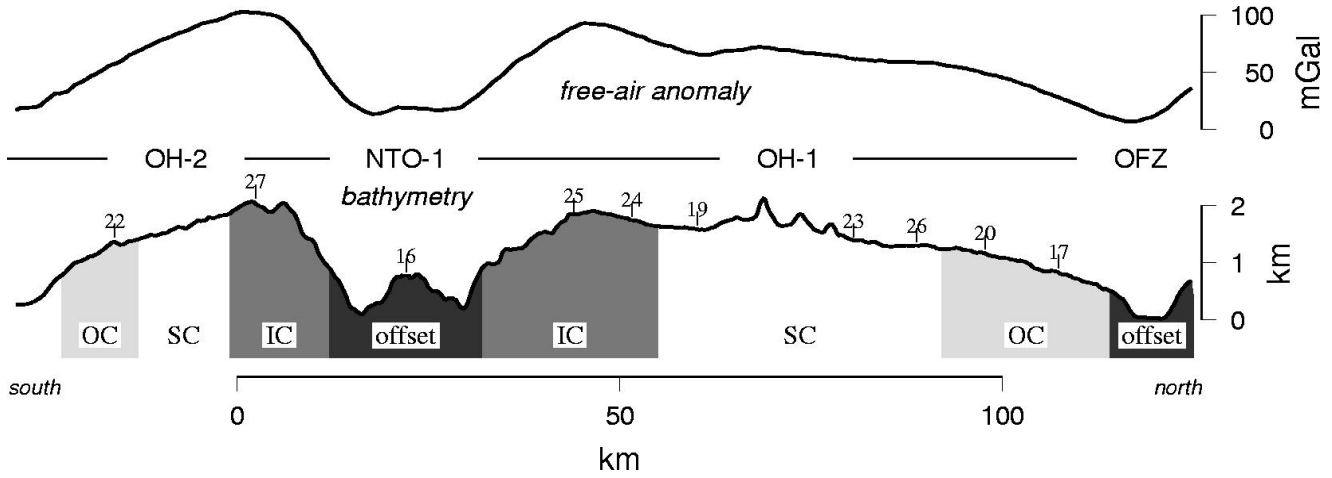

Figure 3. Bathymetry and free-air gravity anomaly along profile MARBE3. Spreading segments OH-1 and OH-2, the nontransform discontinuity (NTO-1), and the Oceanographer fracture zone (OFZ) are labeled. Numbers indicate the location of the ocean bottom hydrophones. Shaded and white areas mark, approximately, the different tectonic sections: segment centers (SC), outside corners (OC), inside corners (IC), and segment discontinuities.

km thick at the segment center and 4.5 km at the OFZ [*Sinha and Louden*, 1983].

OH-2 is a 35-km-long spreading segment bounded on the north by NTO-1 at 34°35'N and on the south by the NTO at 34°10'N (Figure 2b). The U-shaped inner valley is deep (3000-3500 m) and 8 km wide and is flanked by linear rift walls. The eastern rift mountains show a well developed inside-corner high, 990 m deep. No petrological data are available from this segment. However, dives in the adjacent segment to the south, which shares many common morphological and structural characteristics with OH-2 [*Detrick et al*., 1995], have mapped serpentinized peridotites at the inside corner [*Bideau et al*., 1996]. The axial mantle Bouguer gravity anomaly is smaller (25 mGal) than at OH-1, predicting a crustal thickness of 7-8 km [*Detrick et al*., 1995]. Seismic studies indicate a maximum crustal thickness of 6.7 km at the axial center of OH-2 (line A in Figure 2b) [*Hooft et al*., 1999]. The different characteristics between OH-1 and OH-2 have been interpreted in terms of magma supply and thermal structure [*Detrick et al*., 1995; *Thibaud et al*., 1998]: OH-1 may represent a "hot" segment with higher magma supply, while OH-2 may be a "colder" segment with lower magma supply.

NTO-1 laterally offsets segments OH-1 and OH-2 by ~35 km (Figure 2b). It is characterized by a topographic massif elevated 600-700 m from the surrounding seafloor and bounded by two nodal basins 3500 m deep (Figure 3). The massif is similar to those observed at the other offsets of the Oceanographer-Hayes MAR section where serpentinized ultramafics have been observed [*Gràcia et al*., 1997]. The gravity-derived crustal thickness at NTO-1 is 6-7 km [*Detrick et al*. 1995], although this value may overestimate the real thickness if the mean crustal density used in the calculations was too high. Seismic refraction data obtained across the western inactive section of NTO-1 (line E in Figure 2b) show a crustal thickness of 4.5 km and anomalous lower crustal velocities (<6.55 km/s), consistent with a model of fractured, thin crust overlaying partially serpentinized mantle [*Sinha and Louden*, 1983; *White et al*. 1984].

3. Experiment

As part of the Bullseye Seismic Experiment (October-November 1996) [*Detrick et al.,* 1996], an ocean bottom seismic refraction experiment was carried out along a 155-km-long profile along the western rift mountains of OH-1, across NTO-1, and along the eastern rift mountains of OH-2 (profile MARBE3). Ten ocean bottom hydrophones (OBH) were deployed from the OFZ to the discontinuity at 34°10'N (Figures 2b and 3). OBHs 22 and 27 were located along the eastern rift mountains of OH-2, on the outside and inside corner, respectively. OBH 16 was located at the summit of the massif present at NTO-1. The remaining seven instruments (OBHs 25, 24, 19, 23, 26, 20, and 17) were deployed along the western flank of OH-1, two of them along the inside corner, three of them along the segment center, and two along the outside corner. This configuration provided a mean spacing between instruments of 13.7 km (minimum and maximum spacing of 7.6 km and 20.4 km, respectively).

All of the instruments recorded seismic arrivals from 615 air gun shots. The source was the R/V *Maurice Ewing*'s 8420 cubic inch (138 L), 20-air gun array towed at a depth of ~10 m. Shots were fired at an interval of 120 s, providing a seismic trace spacing of 250 ± 35 m. Shot positions were obtained from the shipboard Global Positioning System (GPS) position, corrected for the distance between the GPS antenna and the air gun array (88 m). Accurate locations of the instruments on the seafloor (Table 1) were determined by inverting the direct water wave travel times using the method of *Creager and Dorman* [1982]. The velocity-depth function of the water column was obtained from temperature measurements with expendable bathythermograph probes. The water depths at the relocated position were obtained from the Hydrosweep bathymetry.

4. Seismic and Gravity Data

The seismic data were recorded by each instrument at 200 samples/s and reduced to the standard format of the Society of

Table 1. Instrument Positions

OBH	Latitude, °N	Longitude, °W	*Z*, m	*X*, m	σ_x, m	σ_y, m	φ, deg	Δ*z*, m
22	34.1653	36.8183	1945	-38046	350	16	98	-22
27	34.3291	36.7890	1258	-19622	15	5	9	0
16	34.5025	36.7496	2488	0	559	16	101	-57
25	34.6970	36.7072	1488	21948	16	3	6	-2
24	34.7647	36.6942	1570	29562	16	3	12	27
19	34.8398	36.6743	1705	38104	15	2	12	-30
23	35.0200	36.6317	1937	58500	15	3	12	-16
26	35.0933	36.6153	2031	66762	512	15	99	3
20	35.1718	36.5991	2158	75675	354	16	102	-1
17	35.2572	36.5816	2446	85306	16	2	12	-41

X is the projected position of the instruments along the profile, where the coordinate origin has been arbitrarily assigned to the position of OBH 16. The σ_x, σ_y, φ, are major semiaxis, minor semiaxis, and azimuth of the relocation error ellipses, respectively. Δ*z* is the difference between the depth at the relocated position (*Z*) and the initial depth used in the relocation process (depth at the ship's position at the time of deployment).

Exploration Geophysicists (SEG-Y). The data were corrected for the time drift of the internal clock of the instruments (an average of 24±28 ms/d time drift was measured by comparing the internal clocks with a master clock both before the deployment and after the recovery of each instrument). For plotting and interpretation purposes we applied a band-pass filter of 5-20 Hz to the record sections. No further data processing was required to enhance arrivals. Most of the record sections show a high signal-to-noise ratio (Figure 4), allowing a clear identification of the different phases, which were hand-picked. First arrivals are labeled as *Pg* (turning rays within the crust) and *Pn* (turning rays within the upper mantle). Secondary, high-amplitude arrivals are interpreted as reflections in the crust-mantle boundary (labeled as *PmP*).

A well-defined *Pn* phase was observed at large offsets (>50 km) on some instruments, for example on OBH 22 and 27 (Figures 4a and 4b). These large-offset *Pn* arrivals help to constrain the deeper (upper mantle) seismic structure beneath the NTO-1 and beneath the inside corner of OH-1. The characteristics of the *Pn* arrivals vary along the profile, possibly indicating along-axis changes in the character of the Moho. For instance, data from the instruments that primarily sample the NTO-1 and the inside corner of OH-1 (positive offsets of OBH 22 and 27, positive and negative offsets of OBH 16 and 25, and negative offsets of OBH 24, Figures 4a-4e) do not show a crust-mantle triplication or well-defined *PmP* wide-angle reflections, suggesting the presence of a thick, gradual transition from crustal to mantle velocities beneath the NTO-1. In contrast, data from the instruments that primarily sample the segment center and outside corner of OH-1 (positive offsets of OBH 24 and 19, positive and negative offsets of OBH 23, and negative offsets of OBH 20 and 17, Figures 4e-4g, 4i, and 4j) show a distinct triplication critical distance at which *Pn* becomes the first arrival and *Pg* becomes a secondary arrival (e.g., -35 km in OBH 20), as well as a prominent *PmP* phase (e.g., -40 to -25 km in OBH 23).

Gravity data were collected continuously using the Bell Aerospace BGM-3 marine gravity meter on board the *Maurice Ewing*. Gravity measurements were obtained every 1 s, filtered with a 360-s Gaussian filter, and then the total gravity field was calculated every minute. These 1-min data were merged with ship navigation to obtain a free-air anomaly (FAA) (Figure 3) after Eötvos and instrumental drift corrections.

5. Modeling Procedures

The complexity of the area and the objectives of the study require the data to be modeled using different techniques, according the specific structures we intend to resolve. We used seismic tomographic inversion, ray trace modeling, and gravity modeling to obtain the velocity and density structure of the crust and upper mantle along MARBE3.

5.1. Seismic Modeling

We used the tomographic method of *Toomey et al*. [1994] to invert *P* wave travel times for the two-dimensional (2-D) velocity structure of the upper crust along profile MARBE3. As a starting velocity model, we used a 2-D crustal structure obtained by fitting the first arrivals of five selected instruments using a forward ray trace modeling [*Zelt and Smith*, 1992]. We inspected the resulting model and selected those arrivals corresponding only to rays which turn above the 7.0 km/s isovelocity contour. A subsequent inversion was performed using only crustal arrivals to yield our final velocity model for the upper crustal structure. In the inversion procedure the slowness (i.e., velocity) model is defined on a 160-by-15-km regular grid with a nodal spacing of 0.2 km. The perturbational grid had a spacing of 5 km and 0.36 km in the horizontal and vertical directions, respectively, and the smoothing parameter is 800 in both directions [*Toomey et al*., 1994].

After the upper crustal velocity structure was well-resolved using the tomographic inversion, we used the forward ray trace modeling of *Zelt and Smith* [1992] to match the *PmP* and *Pn* arrival times and to solve, independently, for the lower crustal structure and Moho depth and upper mantle structure. The upper crustal velocity structure (velocities <7.0 km/s) was fixed

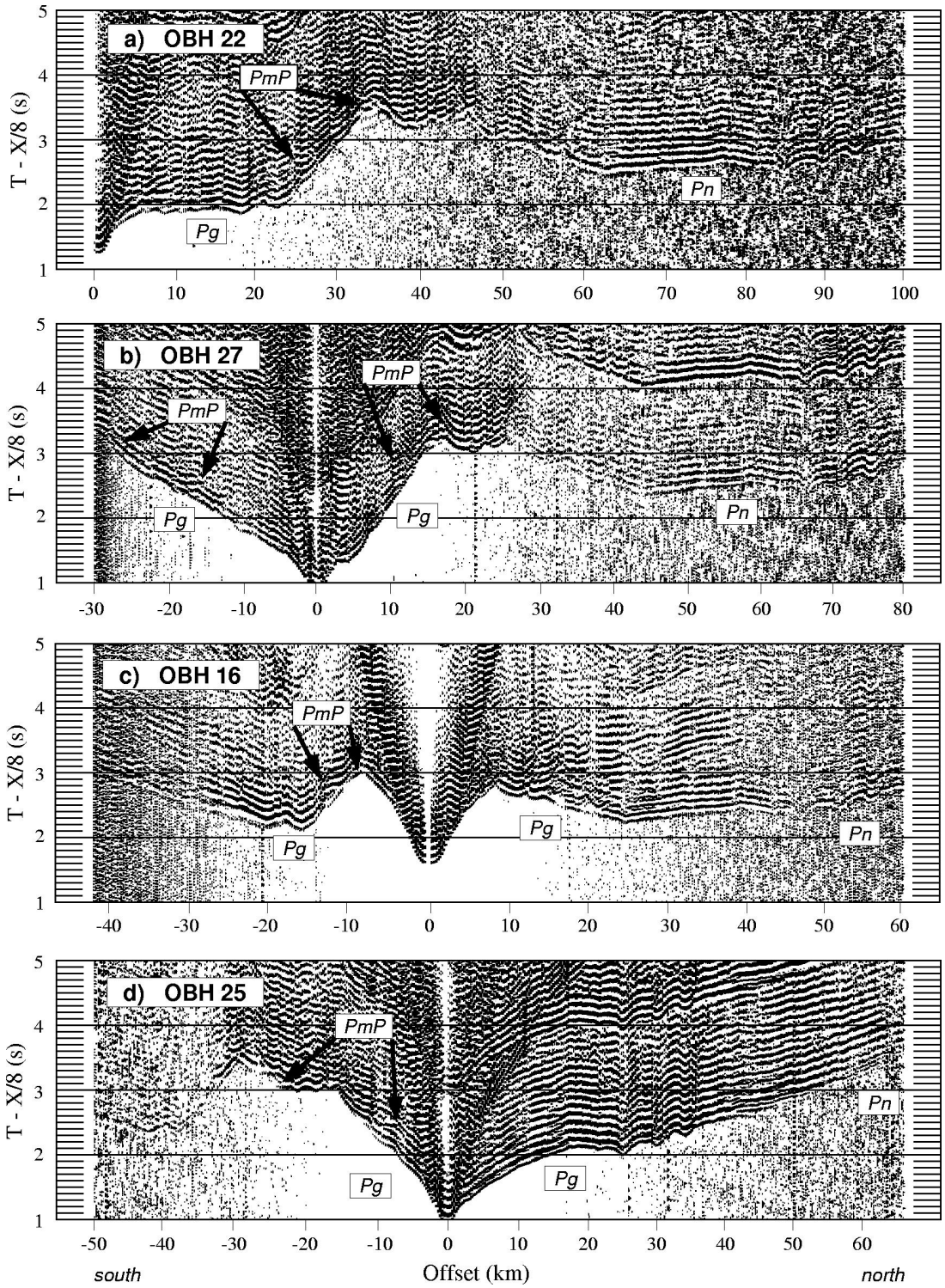

Figure 4. Seismic record sections reduced to 8 km/s, 5-20 Hz band-pass filtered. A power law gain (offset $(km)^{1.5}$) has been applied to the observed amplitudes to enhance the energy at large ranges. Amplitudes have been clipped to a maximum deflection of the trace of 1.5 x trace-spacing. No topographic corrections have been applied. (a)-(j) Consecutive instruments from south to north. Interpreted seismic arrivals have been labeled: *Pg* (turning rays within the crust), *PmP* (reflected rays at the Moho), and *Pn* (turning rays in the upper mantle).

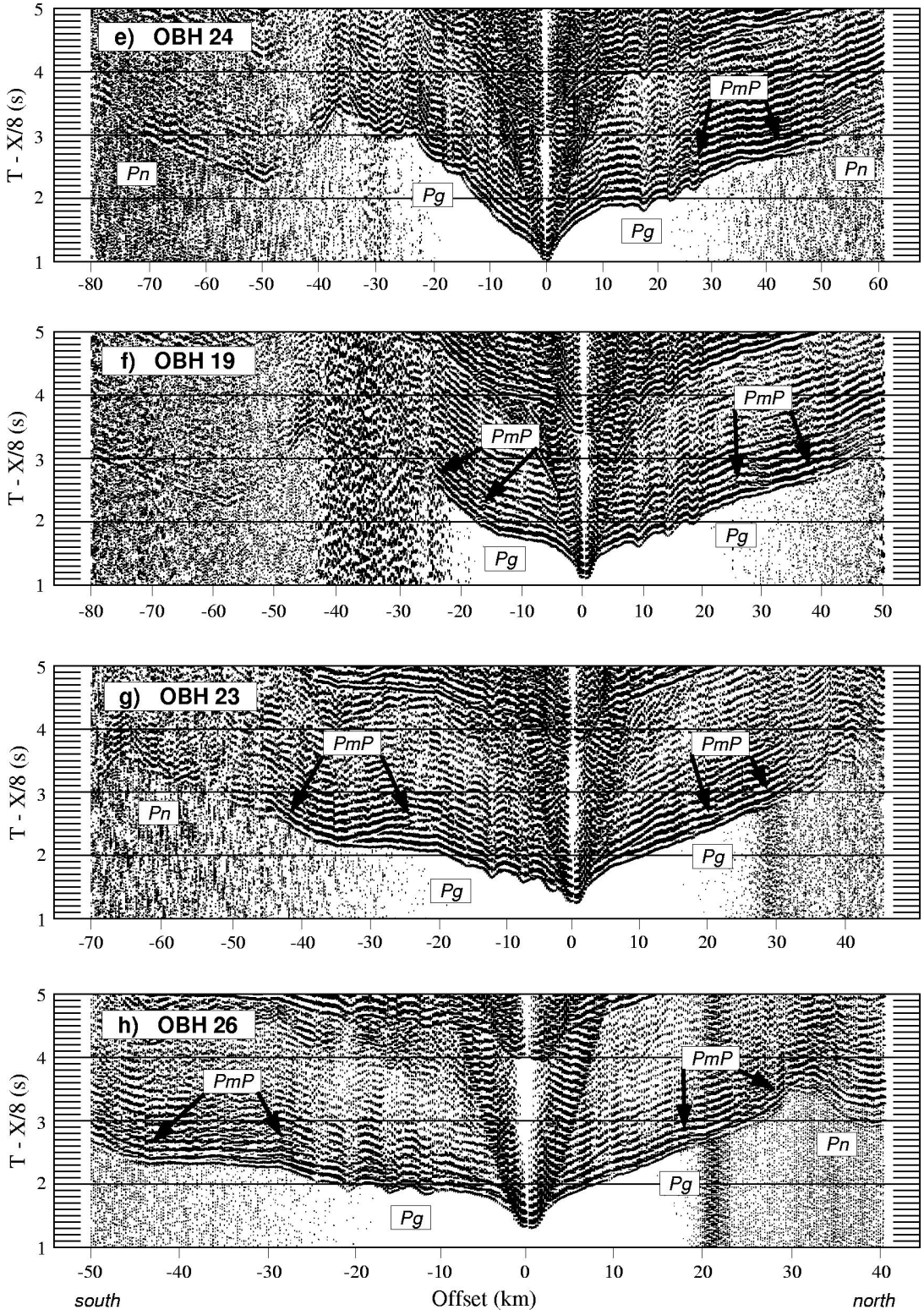

Figure 4. (continued)

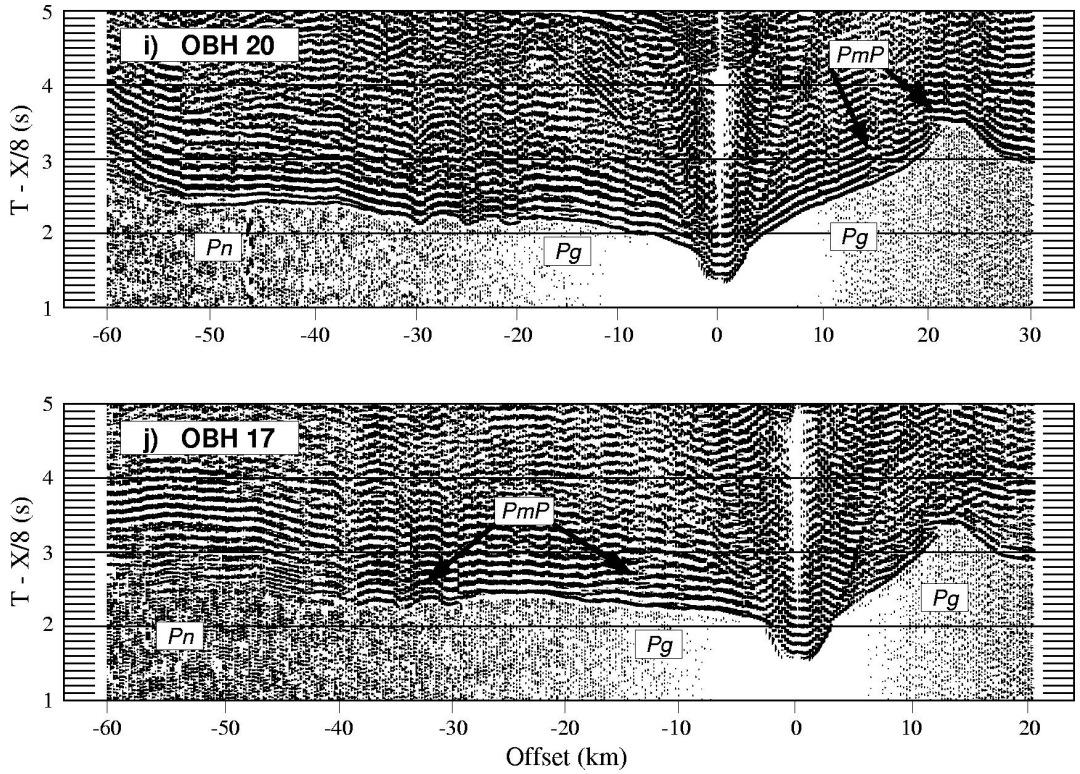

Figure 4. (continued)

during this step, and the lower crustal structure and the shape of the Moho were modified until *PmP* travel times were well fit and the amplitudes of synthetic seismograms were similar to those observed in the record sections. We also checked that the resulting model successfully explains the travel times of *Pg* rays turning within the lower crust. Once the lower crust and the Moho were well constrained, we modeled upper mantle velocities by adjusting the velocities until the *Pn* arrivals were well matched.

5.2. Gravity Modeling

Any seismic model that we obtain must successfully explain not only the *P* wave travel times and amplitudes but also the gravity anomaly along the profile once the velocities are converted to density values. Although our seismic results are fully two-dimensional, we must perform a three-dimensional calculation of the gravity field to account for the lateral effects of the topography in the gravity anomaly. In the absence of additional constraints on the across-axis density structure, we assume that the velocity-density structure below the seafloor along profile MARBE3 is constant in a direction orthogonal to the profile. Thus we create a pseudo-volume with the 3-D bathymetry as upper surface and with density variations in depth and in the north-south direction but not in the east-west direction. From this pseudo-3-D structure we extract selected isodensity surfaces and compute their gravity contribution in the Fourier domain, following the formulation of *Parker* [1972]. The grid dimensions of every isodensity surface are 65 km by 160 km, sampled every 250 m in both directions, and they were mirrored north-south and east-west to simulate periodicity before the Fourier analysis. We retain up to five terms in the Taylor series expansion. The velocity-density relationships that we have used to convert from velocities to densities are discussed in section 6.2.

6. Results

6.1. Seismic Structure

6.1.1. The upper crust. The *P* wave velocity structure of the upper crust was obtained from the tomographic inversion of 1803 *Pg* arrivals (we define upper crust as everything above the 7.0 km/s isovelocity contour, thick white line, Plate 1). The spatial resolution of the model is shown in Figure 5a. The whole profile is well sampled by seismic rays, especially the center of OH-1. The residual travel times between the observed and the predicted *Pg* arrivals (Figure 5b) yield a root-mean-squared (rms) of 31 ms. A comparison of the observed and predicted *Pg* travel times for some instruments is shown in Figure 6.

The velocities in the basement show consistent variations along the profile. The inside corners and segment centers are characterized by seafloor velocities of 3.5-4.0 km/s, while the outside corners and the NTO-1 have slightly lower velocities (3.0-3.5 km/s) in the uppermost crust. Segment OH-2 shows important structural differences between the inside and outside corners. Velocities typical of oceanic layer 3 (>6.5 km/s) are present at shallower depths at the inside than at the outside corner. Segment OH-1 does not show such extreme differences in crustal structure between inside and outside-corner crust.

Both the NTO-1 and the OFZ are characterized by very low upper crustal velocities (V_p=5.5 km/s are not reached until 2.5 km below the seafloor). The transition from the inside corner to the NTO-1 is very different at OH-2 than at OH-1. At OH-2 the

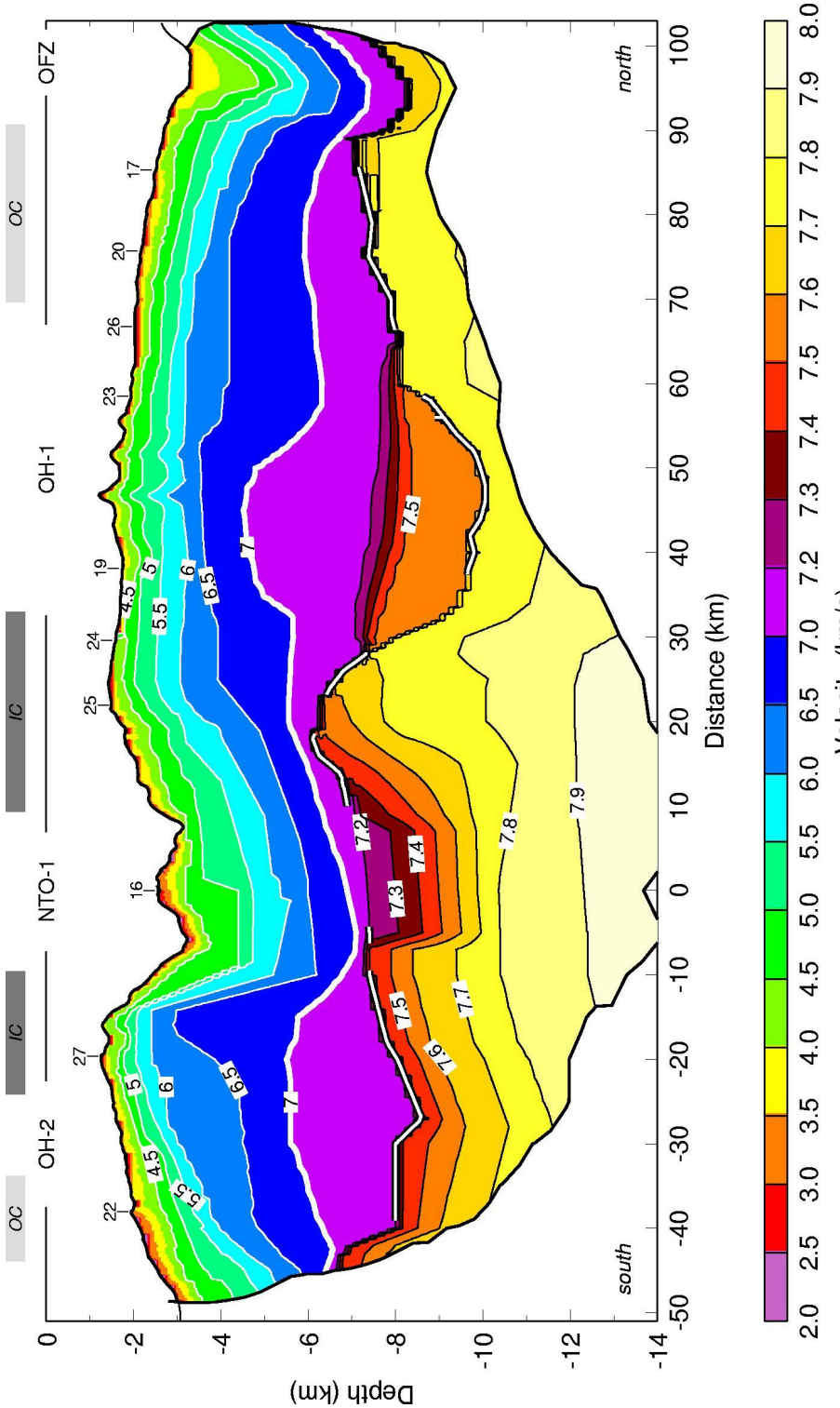

Plate 1. Final *P* wave velocity model. Notation as in Figure 3. White lines are contours every 0.5 km/s, and black lines are contours every 0.1 km/s. Numbers in contours are velocities in km/s. The model is described in the text in three sections: upper crust (limited by the seafloor and the 7.0 km/s isovelocity contour, thick white line), lower crust (limited by the thick white line and the 7.2 km/s isovelocity contour, except between 30 and 65 km where is limited by the 7.6 km/s contour), and upper mantle (everything below the lower crust). Sections of the Moho constrained by *PmP* arrivals are shown in black/white strips. The model is masked out where there is not enough ray coverage

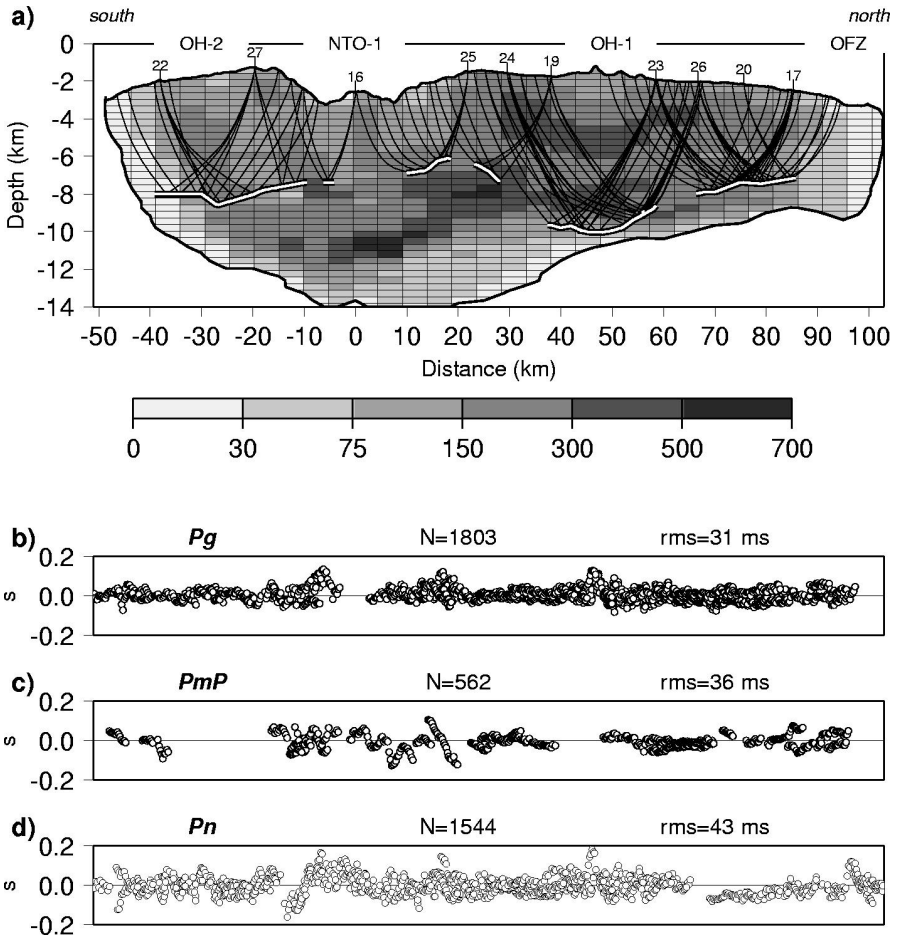

Figure 5. (a) Resolution of the model given by the derivative weight sum parameter [*Toomey et al*., 1994]. One of every 10 rays constraining the Moho (black/white strips) is plotted. Notation is as in Figure 3. The residual travel times ($t_{observed}$-$t_{predicted}$) for (b) *Pg*, (c) *PmP*, and (d) *Pn* arrivals are presented. Horizontal scale is as in Figure 5a. The number of picks (*N*) used in the modeling and the total root-mean-squared (rms) are indicated for each phase.

change from the high-velocity structure of the inside corner to the low-velocity structure of NTO-1 occurs abruptly over a short distance (from -20 to -5 km distance in the velocity model, Plate 1). In contrast, at OH-1 this transition is smoother and more gradual (from 5 to 20 km distance in the velocity model, Plate 1). This contrasting pattern is very apparent in the seismic data. Figure 7a shows data recorded at OBH 27 (located on the inside corner of OH-2) from shots with rays turning in the NTO-1 and its southern wall, and Figure 7b shows the equivalent data recorded in OBH 25 (inside corner of OH-1) with arrivals from the NTO-1 and its northern wall. In both cases, travel times have been corrected for topographic effects. At OBH 27 the arrivals at offsets >13 km (rays entering the crust through the NTO-1) are delayed as much as 0.6-0.7 s with respect to those for shorter ranges (rays entering the crust through the inside corner of OH-2). However, in OBH 25 the increase in travel time from inside-corner to NTO arrivals is gradual.

Our refraction experiment cannot resolve the fine-scale structure of the shallowest crust (uppermost few hundred meters), since seismic energy turning at these depths comes in later than the direct water wave arrival. Detailed velocity analysis reported by Hussenoeder et al. (Upper crustal seismic structure of the slow spreading Mid-Atlantic Ridge, 35°N: Constraints on volcanic emplacement processes, submitted to *Journal of Geophysical Research*, 1998, hereinafter referred to as Hussenoeder et al., submitted manuscript, 1998) from this same area shows that the thickness of layer 2A progressively increases by ~200 m from the segment center toward the OFZ. The depth of the isovelocity contour of 5 km/s (which roughly marks the top of layer 2B (Hussenoeder et al., submitted manuscript, 1998)) clearly increases from the segment center to the north (Plate 1). In particular, the depth increases by ~250 m between OBH 23 and OBH 20, which is the section analyzed by Hussenoeder and coworkers. Thus the uppermost crustal velocity structure along profile MARBE3 is consistent with independent studies and probably does not bias the deeper structure.

6.1.2. The lower crust and the Moho. The thickness and velocity structure of the lower crust along profile MARBE3 were obtained from ray trace modeling the travel times and amplitudes of 562 *PmP* reflections with a final rms of 36 ms (Figure 5c). The *PmP* ray paths and the sections of the Moho

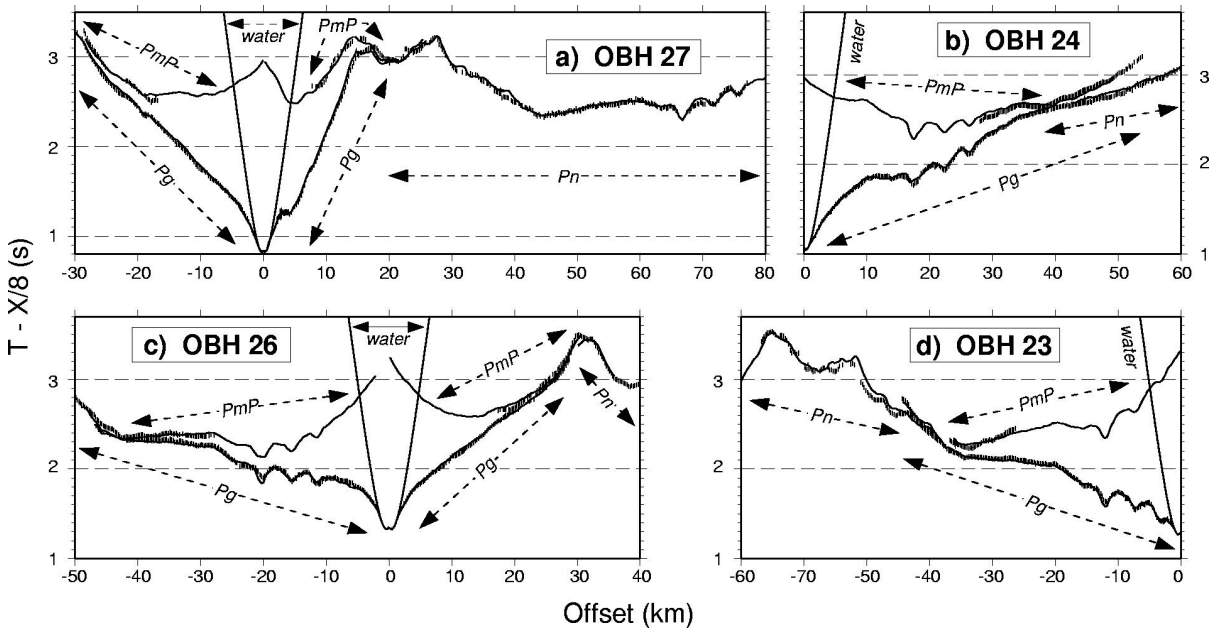

Figure 6. Observed (vertical bars) and predicted (solid lines) travel times for the final velocity model (Plate 1) for some selected instruments. Travel times are reduced to 8 km/s. The height of the observed travel times bars is 50 ms. The different seismic phases are labeled and indicated by dashed arrows. (a) OBH 27 shows the large-offset *Pn* arrivals that constrain the mantle structure beneath the NTO-1 and IC of OH-2 and OH-1. (b) OBH 24 shows the triplication (*Pg-PmP-Pn*) produced at the center of OH-1. (c) OBH 26 shows *PmP* arrivals from the Moho at the center (negative offsets) and at the OC (positive offsets) of OH-1. (d) OBH 23 shows *PmP* arrivals constraining the depth to the Moho at the center of OH-1 and *Pn* arrivals constraining the upper mantle structure beneath the IC of OH-1.

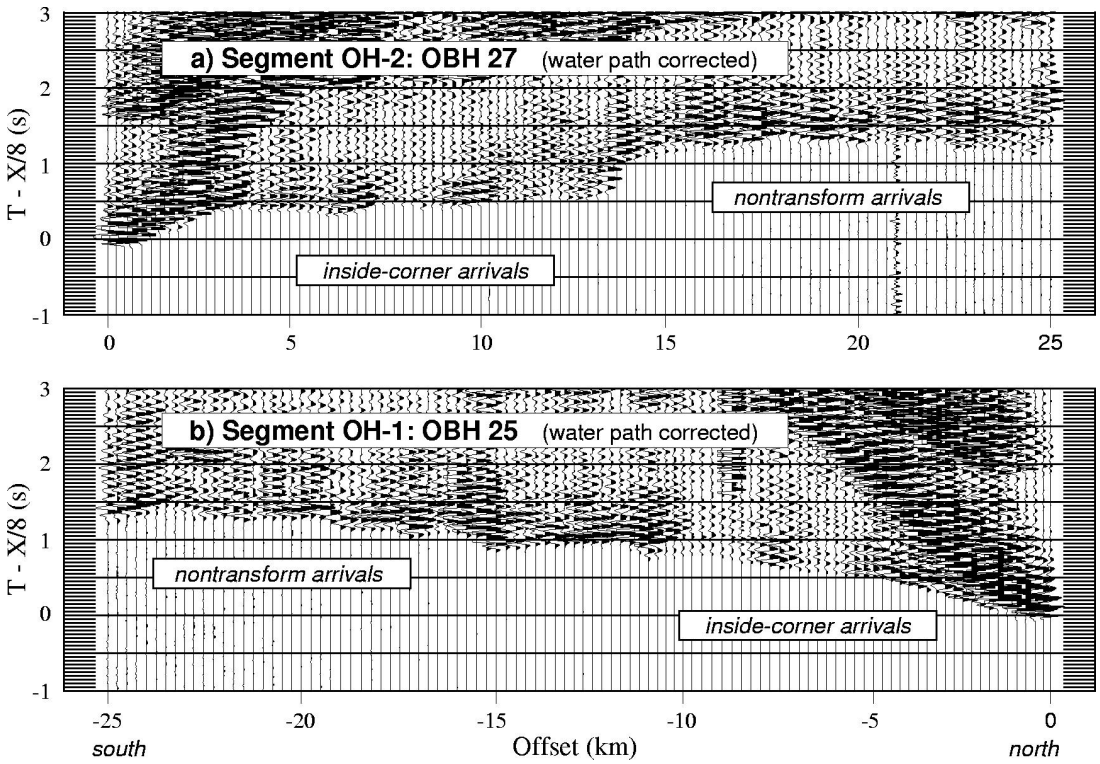

Figure 7. Topography-corrected data for (a) the northern section of OBH 27 and (b) the southern section of OBH 25. Note the abrupt change in travel time in Figure 7a at ~13 km offset. Rays entering the crust at the NTO-1 are 0.6-0.7 s delayed with respect to those rays entering through the inside corner of OH-2. However, Figure 7b does not display such an abrupt delay.

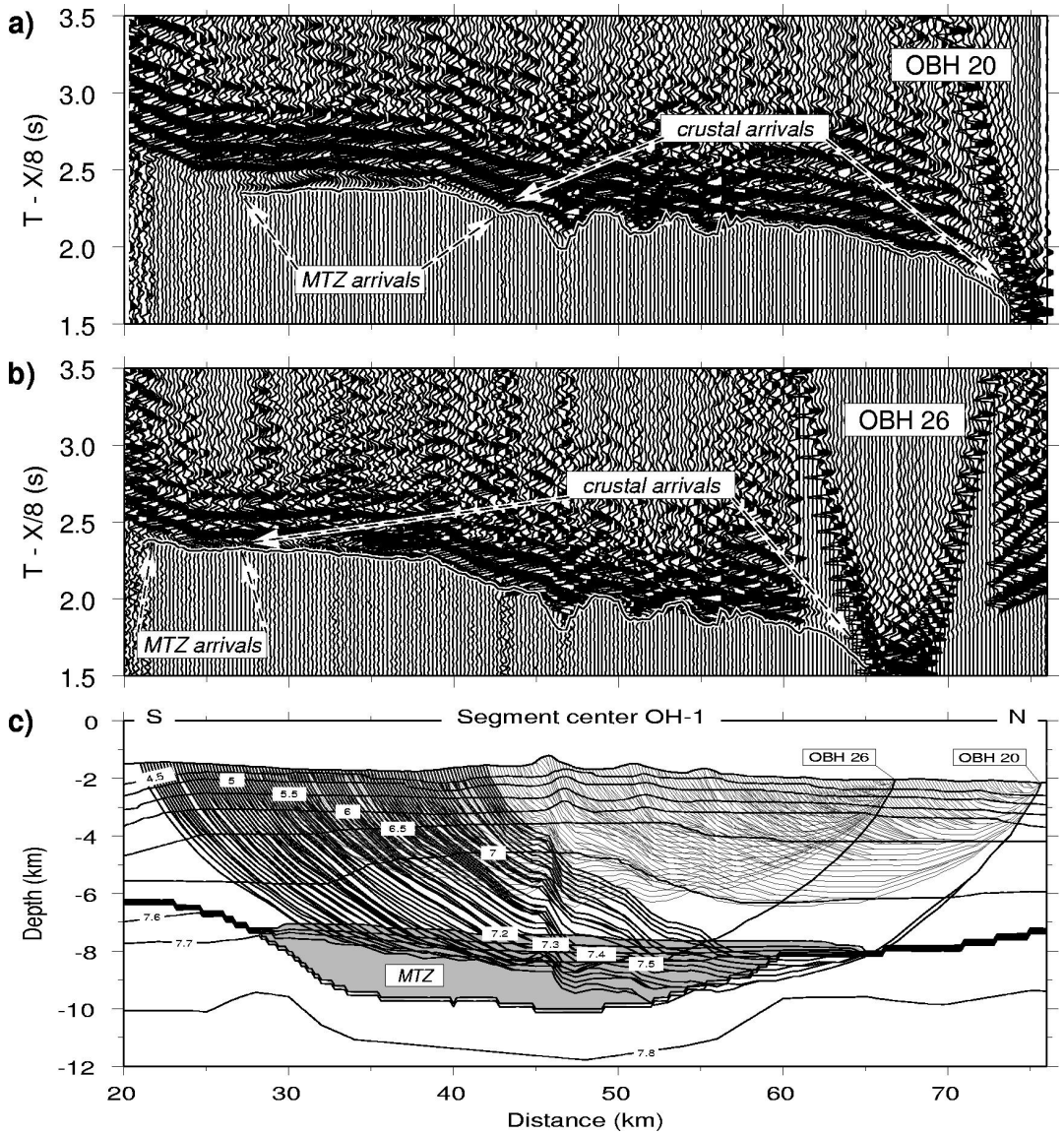

Figure 8. (a) Seismic record section and computed travel times (solid line) for OBH 20. Travel times corresponding to rays turning within the crust are labeled as "crustal arrivals," and travel times corresponding to rays sampling the Moho transition zone are labeled as "MTZ arrivals." (b) same as Figure 8a, for OBH 26. (c) Ray path diagram for OBHs 20 and 26. Only turning rays within the crust (light shaded) and the MTZ (black) are shown. Shaded area labeled as MTZ is the Moho transition zone at the center of OH-1. Velocity contours are annotated in km/s.

constrained by reflecting rays are shown in Figure 5a. Figure 6 also shows the observed and predicted *PmP* travel times for some instruments. Our initial assumption is that the velocity immediately above the seismic Moho does not exceed 7.2 km/s, a reasonable upper limit for lower crustal velocities, and consistent with the travel times of most of the *Pg* arrivals at offsets >30 km (Figure 6). With this assumption, *PmP* arrivals are well fit, and the depth to the seismic Moho was obtained along segment OH-2 and at the inside and outside corners of OH-1.

However, travel times from rays turning within the lower crust at the center of OH-1 (Figure 8) suggest that this section of the profile is characterized by a prominent crustal root with high *P* wave velocities (7.2-7.6 km/s). This root has a maximum thickness of 2.5 km (constrained by *PmP* arrivals, Figure 5a), and its upper boundary is characterized by a velocity gradient of 0.4/s, with velocities from 7.2 to 7.5 km/s. The lower part of the root has velocities from 7.5 to 7.6 km/s. Our best fitting model indicates that *PmP* arrivals come from rays reflecting off the lower boundary of the crustal root. The velocity gradient at the top of this layer is not large enough to produce high-amplitude arrivals with travel times intermediate between *Pg* and *PmP*, as confirmed by comparing the observed record sections with synthetic seismograms (Figure 9).

Segment OH-2 shows only a small crustal thickening near the center of the segment, and the velocities above the seismic Moho are not greater than 7.2 km/s. We have not been able to identify *PmP* arrivals from rays reflecting at any boundary

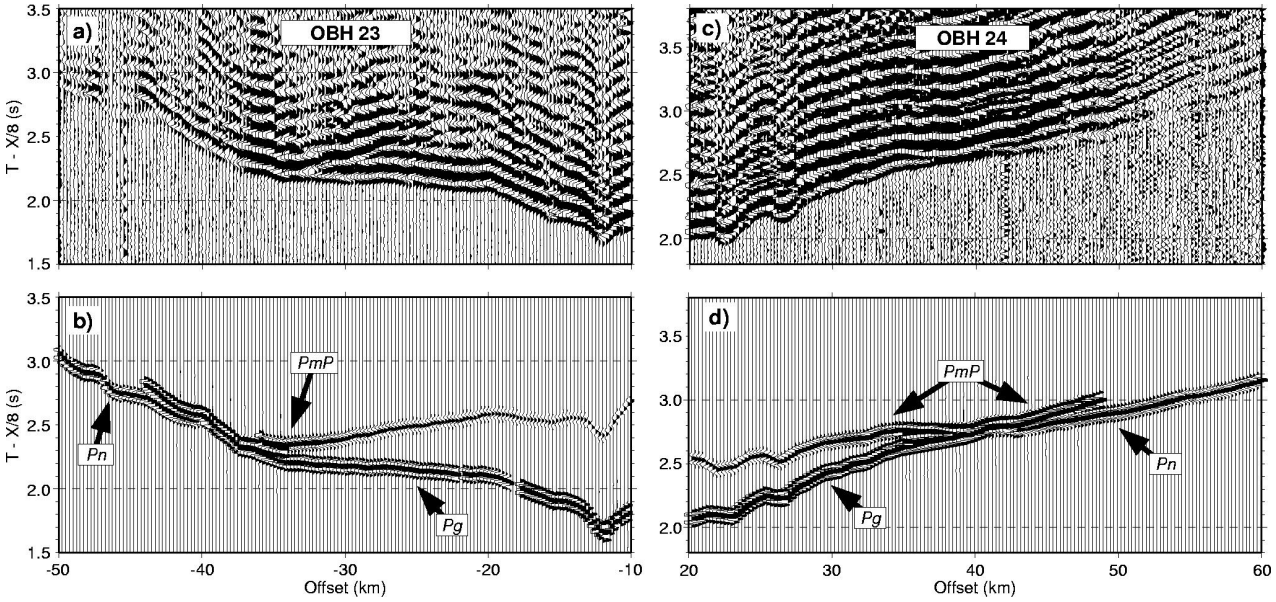

Figure 9. (a) Observed and (b) synthetic seismograms for OBH 23. (c) and (d) Same as Figures 9a and 9b, for OBH 24. In both cases, we show only offsets with arrivals constraining the center of OH-1. Note the good agreement in relative amplitude between the observed record sections and the seismograms predicted by the final velocity model (Plate 1). *PmP* are reflections from the bottom of the Moho transition zone. The model does not predict high-amplitude arrivals from the top of the transition zone.

beneath the NTO-1 (may be due to a wider spacing of the receivers in this region), so the Moho cannot be defined as a seismic reflector along this section of the profile.

6.1.3. The upper mantle. The good quality and large number of *Pn* arrivals recorded allow us to analyze in detail the seismic velocity structure of the upper mantle along profile MARBE3. The 1544 selected *Pn* travel times have been modeled using the ray trace method. Our best fitting model (Plate 1) fits the data with an rms of 43 ms (Figures 5d and 6). The resolution and coverage of rays in the uppermost mantle are shown in Figure 5a. The maximum depth at which we can recover velocity information is 6 km below the Moho at the NTO-1 and the inside corner of OH-1. There is a good resolution from the midsegment of OH-2 to the inside corner of OH-1. Beneath the outside corner of OH-1, ray coverage is also very good, although it is restricted to the upper 2 km of the mantle.

The uppermost mantle velocities beneath the center and outside corner of OH-1 are 7.75-7.80 km/s. However, there is a considerable reduction in the mantle velocities from the midsegment of OH-1 toward the south. Beneath the inside corner of OH-1 we find velocities of 7.5-7.6 km/s immediately below the Moho, and values of 7.9 km/s are observed at 6 km below the Moho. Beneath the NTO-1, the reduction in the upper mantle velocity is even more pronounced, and the initially assumed first-order velocity discontinuity at the Moho disappears along this section of the profile. The uppermost mantle velocity is 7.2 km/s and increases up to 7.9 km/s at 9-10 km subseafloor depth. Beneath segment OH-2, the upper mantle velocities are slightly higher than beneath the NTO-1 but still somewhat low (7.5-7.9 km/s).

6.2. Density Structure

From the observed FAA we have removed the gravity effect of the upper crustal density structure (the lower boundary of the upper crust is taken as the 2950 kg/m^3 isodensity contour, thick white line in Figure 10c), and the effect of mantle-temperature changes associated with a plate-driven flow model [*Phipps Morgan and Forsyth*, 1988] as presented by *Detrick et al.* [1995]. To convert the upper crustal velocities to densities, we used the velocity-density relationship of *Carlson and Raskin* [1984] that accounts for the porosity changes of oceanic layer 2 (hereinafter referred as CR84). The resulting anomaly (residual crustal Bouguer anomaly, RCBA, Figure 10a) represents the gravity signature produced by thickness and/or density variations within the lower crust and upper mantle.

The observed RCBA provides gravity constraints on the seismically derived lower crustal/upper mantle structure. We converted the lower crustal/upper mantle velocity structure to densities using the CR84 relationship (Figure 10b). The computed RCBA (Figure 10a) shows similar features than the observed one (relative minima over the center of the segments, and relative maxima over the discontinuities), but with significantly lower amplitudes.

One possible explanation for such discrepancy is that CR84 underestimates the density of ultramafic rocks with V_p>7.0 km/s. We thus have derived a more realistic velocity-density relationship for the upper mantle (hereinafter referred as VD1, Figure 10b) based in a study of rock samples from the MAR that accounts for the dependence of V_p with the degree of serpentinization β [*Miller and Christensen*, 1997] and accounting for the dependence of seismic anisotropy κ (as defined by *Birch* [1960]) with β (since profile MARBE3 is

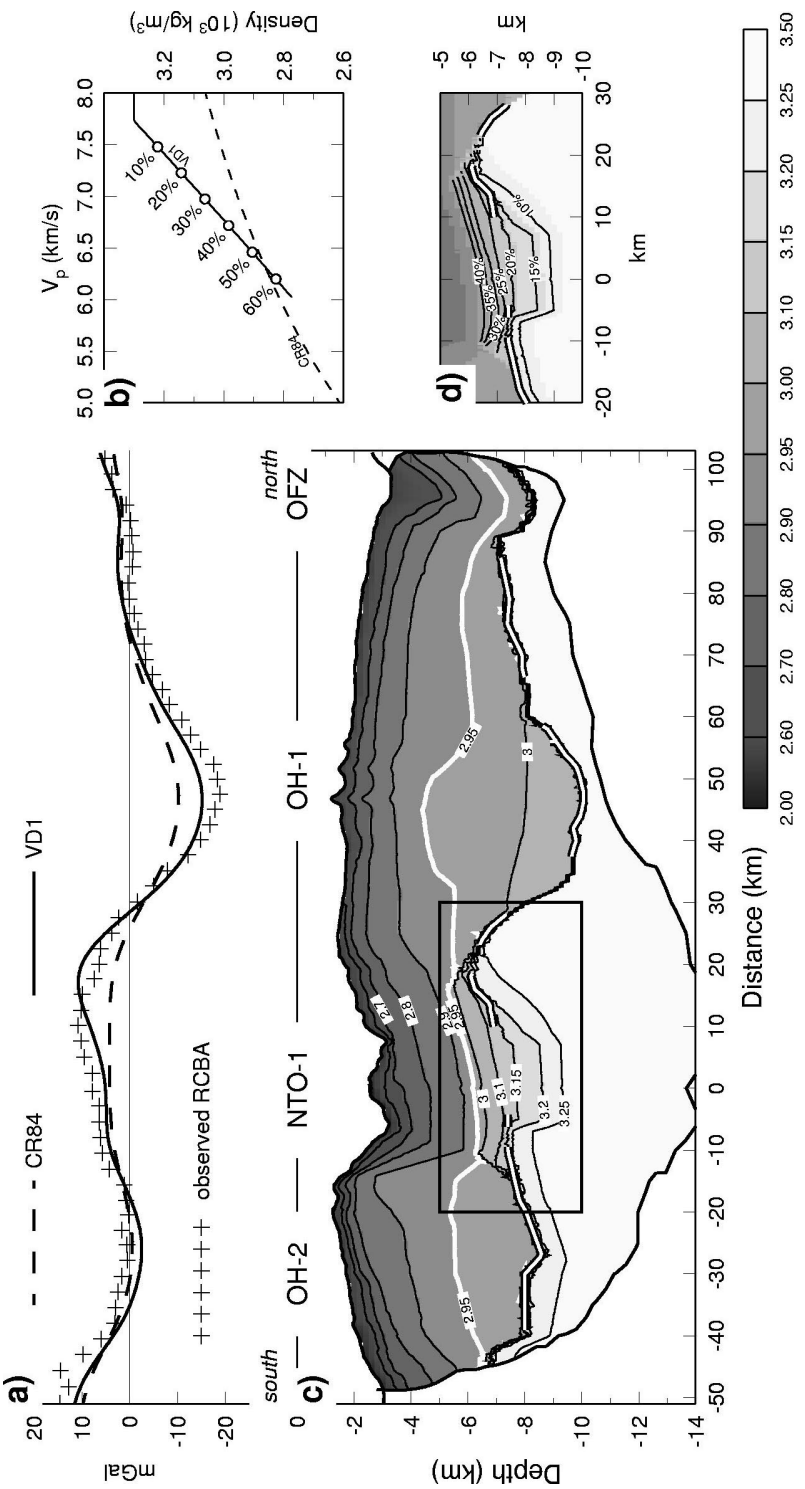

Figure 10. (a) Observed (crosses) and predicted (lines) residual crustal Bouguer anomaly (RCBA) for a variety of density models. The RCBA is obtained by subtracting from the free-air anomaly the gravity signature of the upper crust (densities lower than 2950 kg/m^3) and the effect of mantle-temperature changes. Note the pronounced gravity low over the center of segment OH-1. Dashed line RCBA is obtained from a density model where both crustal and mantle densities are obtained from the CR84 velocity-density relationship (see Figure 10b and text for more details). Solid-line RCBA corresponds to the density model of c), obtained using the VD1 relationship (see b) and text for more details). All curves have zero mean. The rms between observed and predicted RCBA are 4.14 mGal and 2.46 mGal for CR84 and VD1, respectively. (b) Velocity-density relationships. Dashed line (CR84) corresponds to that of *Carlson and Raskin* [1984] for lower oceanic crust, and solid line (VD1) is derived from the relationships of *Miller and Christensen* [1997] and *Horen et al.* [1996] to account for the degree of serpentinization and seismic anisotropy. Open circles denote percentage of serpentinization. (c) Final density model. Crustal and mantle densities were obtained using CR84 and VD1, respectively, and the VD1 relationship was also used for the lower crust (V_P>7.0 km/s) beneath the NTO-1. Contours are labeled in 10^3 kg/m^3 (note that contour interval is not constant). Thick white line (isodensity contour of 2950 kg/m^3) separates the upper from the lower crust. Solid box indicates the section presented in Figure 10d. (d) Detail of the density model (see location within the profile in Figure 10c). Annotated black contours indicate percentage of serpentinization. Sections of the Moho constrained by *PmP* arrivals are shown in black/white strips in Figures 10c and 10d.

oriented orthogonal to the spreading direction, we are measuring the *P* wave velocity of the upper mantle in the slowest direction [*Christensen*, 1984]) as reported by *Horen et al*. [1996]. Figure 10b shows that for a given *P* wave velocity, VD1 predicts a higher density for peridotites less than 40-50% serpentinized than that of CR84. Combining CR84 and VD1 for the crustal and upper mantle sections, respectively, we obtain a density model (Figure 10c) that considerably improves the fit of the observed RCBA (Figure 10a).

Serpentinite outcrops commonly at the NTOs along this section of the MAR [e.g., *Gràcia et al.,* 1997], and it seems likely that a significant portion of the seismically defined "crust" in the NTO is actually partially serpentinized peridotite. Thus we have used the VD1 relationship to convert velocities to densities at the NTO-1 below the 7.0 km/s isovelocity contour. The model predicts that at least ~40% of serpentinization occurs ~3.8 km below the seafloor (Figure 10d). This model improves the fit of the RCBA at the NTO-1 by ~3 mGal when compared with a model where serpentinization of the NTO-1 is restricted to depths >5 km below the seafloor.

7. Discussion

7.1. Segment OH-1

7.1.1. Segment center. Figure 11a shows a one-dimensional velocity-depth profile extracted at 45 km distance on the model. The upper ~6 km have a seismic structure similar to that observed in most of the ocean basins [e.g., *White et al*., 1992]. The upper 2 km of the crust are correlated with seismic layer 2, with a mean velocity gradient of ~1.5/s. This layer is assumed to consist of extrusive basalts and sheeted dikes. We have tentatively placed the limit between extrusives and intrusives at ~0.5 km below the seafloor on the basis of a slight decrease in velocity gradient at that depth. This interpretation is consistent with the results of Hussenoeder et al. (submitted manuscript, 1998), who locate the transition from extrusives to dikes at 0.3-0.5 km depth in the western rift mountains of OH-1. Layer 3, ~4 km thick and with velocities increasing from 6.5 km/s at the top to 7.2 km/s at the bottom, has a lower velocity gradient (~0.2/s) than layer 2, and it is probably composed of gabbros.

One of the most interesting results of this study is the evidence for a high-velocity crustal root at the center of OH-1. Below layer 3, the seismic and gravity data require the presence of a layer with velocities intermediate between crust and mantle (from 7.2 to 7.6 km/s) and density of ~3000 kg/m^3. We refer to this crustal root as the Moho transition zone. A similar structure has also been observed at the center of a slow spreading segment in Mesozoic Atlantic crust [*Henstock et al*., 1996]. The bottom boundary of the transition zone is modeled as a first-order velocity discontinuity, a seismic reflector which is the origin of the *PmP* arrivals. The unusual velocities of the transition zone are too high to be consistent with a gabbro section and too low to represent normal peridotitic mantle. Similar subcrustal velocities have been reported in different tectonic environments. The high velocities (>7.2 km/s) in the lower crust along the U.S. Atlantic continental margin [*Holbrook et al*., 1994] have been interpreted as igneous rocks with a high proportion of olivine component, derived from melting initiated at high pressures (4 GPa) and high mantle potential temperatures (1500°C) [*Kelemen and Holbrook,* 1995]. However, such conditions are unlikely to occur in normal mid-ocean ridges, where decompression melting in passive mantle upwelling takes place at a potential temperature of 1300°C and an average pressure of ~1 GPa [e.g., *McKenzie and Bickle*, 1988].

The velocities observed in the Moho transition zone near the center of segment OH-1 are consistent with partially serpentinized peridotites [*Christensen*, 1966]. However, it is unlikely that this represents a serpentinized body. The gravity low associated with this thick transition zone is the off-axis extension of a bull's-eye gravity low centered on segment OH-1 [*Detrick et al*., 1995], indicating that this feature formed on-axis (as the crustal root described by *Hooft et al*. [1999]). Morphological and petrological observations indicate that the central portion of OH-1 has been magmatically robust over the past few million years [*Bideau et al*., 1996], and microseismicity studies in this area suggest a hot, ductile lower crust below 3-4 km depth in the axial zone [*Barclay et al*., 1998]. It is thus unlikely that near the center of segment OH-1 seawater has penetrated to crustal depths of >6 km, necessary to explain the origin of this thick Moho transition zone as a body of serpentinite.

We believe it is more likely that this feature represents an alternating sequence of gabbro sills and dunites similar to that observed above the Maqsad diapir in the Oman ophiolite [*Nicolas and Boudier,* 1995]. In Oman, this several hundred meters thick Moho transition zone is thought to form when porous flow of melt rising from below reaches a permeability barrier, forming sills which crystallize as gabbroic cumulates [*Kelemen et al*., 1995, 1997; *Korenaga and Kelemen*, 1997]. The lower levels of the Oman transition zone are primary dunitic, while the upper levels are rich in gabbro. A similar Moho transition zone has been described in the Bay of Islands ophiolite complex [e.g., *Karson et al.*, 1984]. In that area the Moho is a gradual transition from mafic to ultramafic rocks. The proportion and thickness of ultramafic layers within the transition zone increase with depth, and the main lithologies are dunite, olivine-gabbro, and gabbro. This type of Moho transition zone produces seismic signatures similar to those observed in marine seismic experiments [*Collins et al*., 1986].

The Oman and Bay of Islands Moho transition zones have seismic structures[*Christensen and Smewing*, 1981; *Karson et al.*, 1984] similar to that observed at the transition zone of OH-1: below layer 3, numerous grabbroic intrusions within the dunites may produce higher velocities (7.2-7.4 km/s) than that of gabbroic rocks; while the decrease in the number of sills with depth may produce velocities (7.4-7.6 km/s) closer to that of mantle peridotites. The differences in the thickness of the transition zones between OH-1 and the ophiolite complexes may be due to differences in tectonic setting, spreading rate, and thermal structure [*Sleep*, 1975].

In our model the seismic Moho at the center of OH-1 corresponds to the base of a transition zone composed of gabbros alternating with dunites. If dunites are formed by porous flow [*Kelemen et al*., 1995], instead of representing cumulates [*Takahashi*, 1992], the depth to the Moho at the center of OH-1 may overestimate the total igneous crustal thickness. Assuming that the measured seismic velocities within the transition zone are proportionally controlled by the fractions of gabbros and dunites per volume unit, we estimate that the Moho transition zone is composed of ~70-80% of igneous

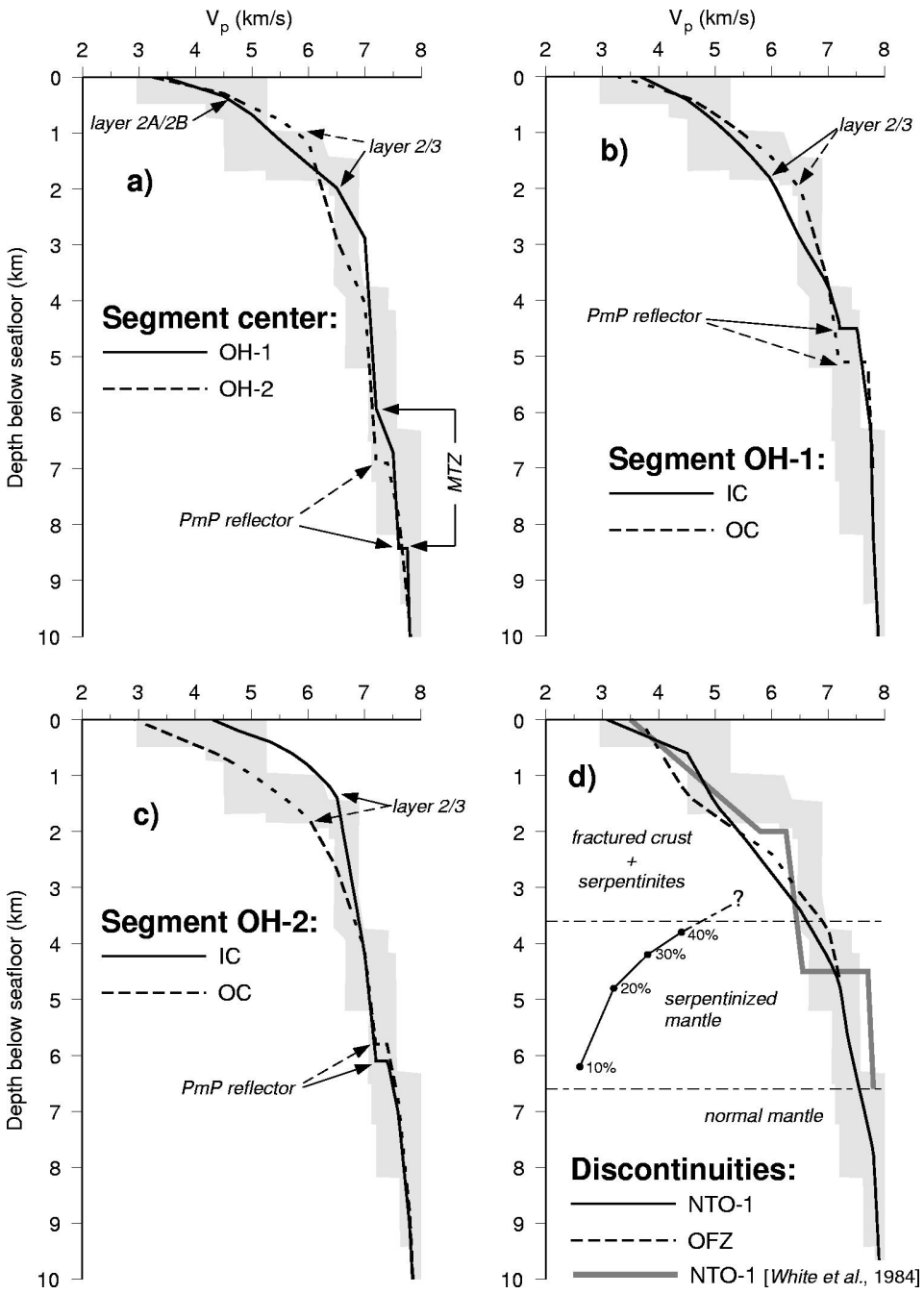

Figure 11. Velocity-depth profiles at several representative locations. Shaded backgrounds show, for reference purposes, the compilation of profiles in 1-7 Ma Atlantic crust of *White et al*. [1992]. Main boundaries are labeled and indicated by arrows. (a) Center of segments OH-1 and OH-2, profiles extracted at 45 and -25 km in the model, respectively. Note that the *PmP* reflector at OH-1 is located at the base of the Moho transition zone (MTZ). (b) Inside and outside corners of OH-1, profiles extracted at 20 and 75 km in the model, respectively. (c) Inside and outside corners of OH-2, profiles extracted at -15 and -40 km in the model, respectively. (d) Segment discontinuities NTO-1 and OFZ, profiles extracted at 0.5 and 97 km in the model, respectively. Structure at the inactive section of NTO-1 given by *White et al*. [1984] is shown for comparison as thick shaded line. Thin solid line with numbers indicates the percentage of serpentinization in the upper mantle beneath the NTO-1; the depth interval is indicated by the horizontal, thin dashed lines, although serpentinization may also occur at shallower levels.

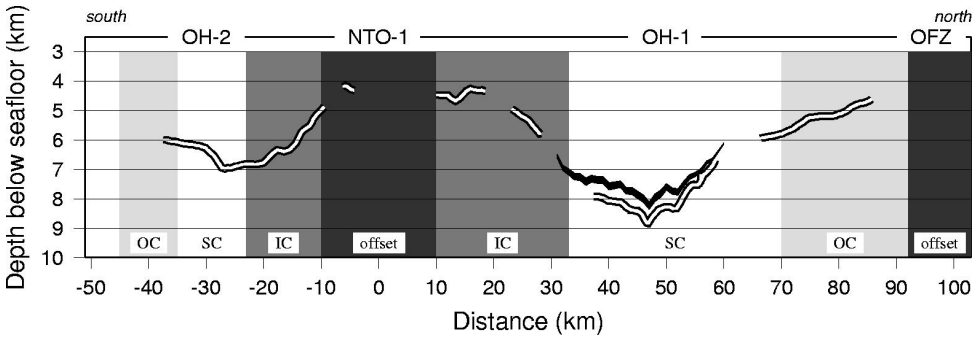

Figure 12. Depth to the *PmP* reflector along the profile (black/white strips), which is considered as igneous crustal thickness except between 30 and 65 km distance. Within this section, the *PmP* reflector is the lower boundary of a Moho transition zone, possibly comprised of ~70-80% of igneous gabbroic sills interlayered with dunites. The estimated crustal thickness at this section (see text for details) is bounded by the black line. Labeling and shaded areas are as in Figure 3.

gabbro sills and 20-30% of dunites (using a gabbro velocity of 7.2 km/s, the maximum observed in our model in the lower crust, and a dunite velocity of 8.2-8.7 km/s [*Karson et al*., 1984]). The subseafloor depth to the *PmP* reflector can be considered a measure of the igneous crustal thickness along the profile except at the center of OH-1. In this area we estimate the igneous crustal thickness as (depth to the *PmP* reflector) minus (20-30% of the thickness of the transition zone) (Figure 12, black band), reaching a maximum value of 8.1-8.3 km (comparable to the 8.2 km at the axial center of OH-1 [*Hooft et al*., 1999]).

7.1.2. Inside and outside corners. Crustal structures at the inside and outside corners of OH-1 are, in general, very similar (Figure 11b). Uppermost crustal velocities are slightly higher at the inside (3.5-4.0 km/s) than at the outside corner (3.0-3.5 km/s). This may indicate that the inside corner has been stripped, at least in part, of the extrusive layer as it is rafted into the rift mountains. However, at both sites, velocities >6.0 km/s are observed at depths >2 km, suggesting that layer 2 is present at both ends. Crustal thicknesses present some interesting differences (Figure 12). The mean crustal thickness is 5.3±0.3 km at the outside corner and 4.9±0.6 km at the inside corner (errors are one standard deviation), suggesting somewhat thinner inside-corner crust. However, the large variability in crustal thickness in both areas (5.9 to 4.6 km at the outside corner, and 6.4 to 4.3 km at the inside corner) makes it difficult to interpret these mean values. A better parameter is the rate of thinning toward the segment ends. At the outside corner the crust thins at a rate of ~65 m/km, while at the inside corner it thins at a rate of ~163 m/km (Figure 12). This difference may be due to the uplift and tectonic thinning of the inside-corner crust [*Tucholke and Lin*, 1994; *Escartín and Lin*, 1998]. Also, the thinnest crust is not located where the inside corner is shallowest but along the flanking wall. This is consistent with the observation that gravity highs at oceanic core complexes are not centered with respect to their morphology but are shifted toward the spreading axis and transform sides [*Blackman et al.*, 1998].

We find large differences between the inside and outside corners of OH-1 in the structure of the uppermost mantle. Beneath the outside corner, mantle velocities are normal (>7.7 km/s), while at the inside corner we find velocities of 7.5-7.6 below the Moho. We postulate that these low velocities reflect a ~15-km-long transition from the mantle beneath the center of OH-1 to the partially serpentinized mantle beneath the NTO-1. At the wall of the inside corner of OH-1 the gravity modeling suggests the presence of peridotites with 25-40% serpentinization right above the seismic Moho (Figure 10d). Thus we postulate that at least in some part of the inside corner of OH-1, the Moho corresponds to an alteration front.

7.2. Segment OH-2

7.2.1. Segment center. The seismic structure at the center of OH-2 is distinctively different from that at OH-1 (Figure 11a). We infer a thinner extrusive layer on the basis of a shallow (~1 km) decrease of the velocity gradient. The center of OH-2 does not have anomalous velocities in the Moho transition zone. The maximum velocity above the Moho is 7.2 km/s, which is modeled as a first-order discontinuity between the igneous crust and the mantle. The off-axis mean crustal thickness at the center of OH-2 is 6.6±0.3 km (minimum and maximum thickness of 6.0 km and 7.0 km, respectively; Figure 12), similar to that observed at the axial center of OH-2 (6.7 km [*Hooft et al*., 1999]). Mantle velocities below OH-2 are somewhat low, and that may be considered as some type of transition zone between the crust and the mantle. However, the *PmP* reflector coincides with the 7.2 km/s isovelocity contour. To be consistent with our interpretation of the structure of OH-1, we do not favor the existence of a transition zone beneath OH-2, although it cannot be totally ruled out.

7.2.2. Inside and outside corners. The structures at the inside and outside corners of OH-2 display important differences (Figure 11c). The inside-corner crust is consistently faster than the outside-corner crust within the upper 4 km. At 1.5 km depth the inside corner has a velocity of 6.5 km/s. This, if compared with the structure at the outside corner and the center of the segment, suggests that layer 2 at the inside corner has been partially removed. Although layer 2 at the inside corner has a velocity gradient resembling an extrusive section, we do not exclude the possibility that the upper 1.5 km of the crust at the inside corner are also composed of dikes and/or gabbroic rocks with reduced velocities due to fracturing, as observed in Hole 735B [*Dick et al*., 1991; *Muller et al*., 1997].

Crustal thickness at the inside corner of OH-2 varies between 5.2 and 6.8 km, with a mean value of 6.2±0.5 km (Figure 12). The rate of thinning is 161 m/km, similar to that at the inside corner of OH-1, with the thinnest crust occurring at the nontransform wall, shifted with respect to the shallowest point. The higher velocities and the shoaling of the isovelocity contour of 6.5 km/s at the inside corner (Plate 1) suggest that inside-corner crust is thinner than outside-corner crust. However, there

are not enough *PmP* reflections from the outside corner to confirm this hypothesis.

7.3. Nontransform Offset NTO-1 and Oceanographer Fracture Zone

The crustal structures at NTO-1 and the OFZ are clearly anomalous with respect to Atlantic-type ocean crust [e.g., *White et al*., 1992] (Figure 11d). Both velocity-depth profiles lack the distinct change in velocity gradient that characterizes oceanic layers 2 and 3, and they show a nearly constant velocity gradient within the upper 4-5 km. This type of structure may be interpreted as thin, intensely fractured and altered basaltic crust overlaying partially serpentinized mantle [e.g., *Minshull et al*., 1991; *Detrick et al*., 1993].

Although velocities at depths greater than 4 km at NTO-1 are similar to those observed in the Moho transition zone at the center of OH-1, the densities required to match the gravity field suggest the presence of serpentinized peridotites. Our preferred model (Figure 10) predicts that serpentinization reaches 10% at ~6.2 km below the seafloor and at least 40% at ~3.8 km (Figure 11d). The highly fractured upper crustal section may enhance hydrothermal circulation, thereby producing serpentinites above their stability field (400-500°C) [*Coleman*, 1971; *O'Hanley*, 1996]. Although serpentinization may preferentially occur along fractures, at temperatures of ~300°C the partially serpentinized section of the mantle displayed in Figures 10c and 10d may have formed in a period of <2 Myr [*Macdonald and Fyfe*, 1985]. Our velocity and density models do not allow us to discriminate the presence of serpentinites at depths shallower than ~3.8 km. However, we argue that they should be present at shallow levels, since they have been observed at the seafloor in the nearby NTOs [*Gràcia et al*., 1997]. Thus 3.8 km may be an upper limit for the thickness of the igneous crust at the NTO-1.

The velocity structure at the OFZ within the upper 4 km is very similar to that at the NTO-1 (Figure 11d), indicating that the crust is highly fractured. The lack of seismic coverage below 4 km does not allow us to analyze the structure of the upper mantle at this section of the profile. The similar crustal structures of NTO-1 and OFZ suggest that even small NTOs should be considered fundamental boundaries of ridge magmatic segmentation.

7.4. Geological and Tectonic Implications

7.4.1. Crustal thickness variations and source of the bull's eye gravity low. Our results provide constraints on the relationships between crustal thickness, magma supply, gravity anomalies, and axial morphology. The mean crustal thicknesses of OH-1 and OH-2 are 6.0±1.2 km and 6.1±0.7 km, respectively, where uncertainties are standard deviations and reflect the large crustal thickness variability along both segments (mean crustal thicknesses have been measured between -45 and -10 km model distance for OH-2 and between 10 and 90 km for OH-1, Plate 1). Thus our results suggest that both segments have similar average crustal thicknesses and magma supply (and thus similar average thermal structures), in contrast to what has been inferred from morphology and gravity observations [*Detrick et al*., 1995; *Thibaud et al*., 1998]. For the same magma supply, OH-1 has a larger off-axis along-segment crustal thickness variation (~3.3 km) and is thicker at the center (~8.2 km) than OH-2 (~1.8 km and ~7 km, respectively). These differences may explain the contrasting gravity anomalies and axial morphologies of segments OH-1 and OH-2 without invoking magma supply differences. We find that the off-axis gravity signature along profile MARBE3 can be entirely explained by crustal thickness and density variations. The off-axis crustal thickness variations are the same order as those observed on-axis [*Hooft et al*., 1999]. Our results suggest that rather than having a higher magma supply than OH-2, OH-1 is characterized by a more focused supply of melt from the mantle, or less efficient along-axis magma transport at crustal levels. This may reflect the proximity of OH-1 to the large-offset Oceanographer transform.

7.4.2. Tectonic alteration of the ocean crust at the inside corners. The rate of crustal thinning from the segment center to the inside corner observed at both segments is consistent with the hypothesis that the inside-corner crust is tectonically modified when rafted from the axial valley to the rift mountains [e.g., *Tucholke and Lin*, 1994; *Escartín and Lin*, 1998]. Furthermore, the model of *Tucholke and Lin* [1994] predicts that inside-corner faults develop at low angles in both across-axis and along-axis directions, resulting in a transition in the style of faulting at the segment center. The isovelocity contour of 6.5 km/s at OH-2 (beneath OBH 27) dips from the inside corner to the segment center with an angle <20° (Plate 1) and probably marks the along-isochron limit of the faulting pattern between the inside corner and segment center. We do not observe important differences in the depth to the seismic Moho between the inside and outside corners at both segments. However, the Moho beneath the inside corner may correspond to an alteration front, and thus the igneous crust may be thinner at the inside than at the outside corners.

The inside-corner crust of OH-2 has higher average velocities than the inside-corner crust of OH-1, while both outside corners have similar velocity structures. This observation is consistent with the hypothesis that the axial extrusive layer at OH-2 may thicken from north to south, while at OH-1 it may thicken symmetrically from the segment center toward the ends. If lateral magma transport away from the injection zone is efficient [*Fialko and Rubin*, 1998], at OH-2 magma would migrate southward away from its northern end, where the axial crust is thicker [*Hooft et al*., 1999] and the axial valley is shallower [*Detrick et al.,* 1995]. In contrast, at OH-1 magma would migrate northward and southward away from the segment center (Hussenoeder et al., submitted manuscript, 1998). According to the model of *Tucholke and Lin* [1994], when the axial crust is rafted to the rift mountains the basaltic carapace may be totally stripped from the inside-corner crust at OH-2 but not at OH-1.

We observe significant differences in the velocity structure across the inside corner-NTO-1 intersections. The velocity structure changes abruptly across the southern wall of the NTO-1. This sharp transition probably bounds the portion of the segment that is tectonically modified at the inside corner. In contrast, the northern wall of the NTO-1 is associated with a gradual transition from the offset to the inside corner of OH-1. Although the origin of this asymmetric pattern is unclear, we speculate that it may be related to the growth and southward propagation of OH-1 [*Deplus et al*., 1998].

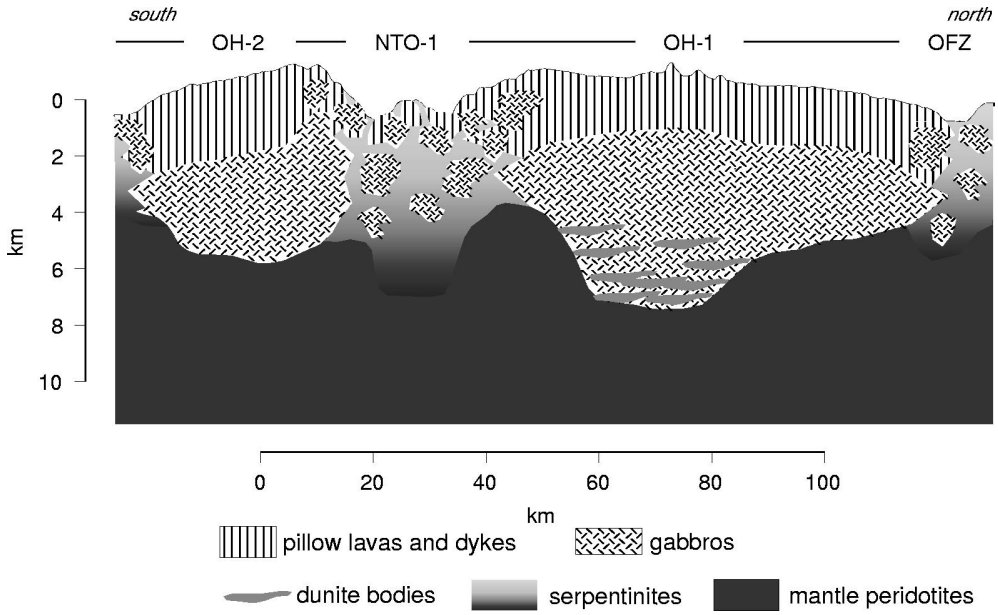

Figure 13. Sketch showing a geological interpretation of our results. The main features are discussed in the text. Thickness and extension of the different geological units are rough approximations.

7.4.3. The nature of the seismic Moho at slow spreading ridges. In the absence of direct deep drilling of the Moho in modern oceanic crust the correlation between lithology and seismic velocities at subcrustal levels remains unresolved, and only extrapolations from ophiolite complexes can be made (with the caveat of the uncertainty in the spreading rate and thermal structure of the paleoridge). The seismic Moho, defined as the lithospheric section in which *P* wave velocities increase from ~7 to ~8 km/s (abruptly or gradually), can be a serpentinization front or a petrological boundary between mafic and ultramafic rocks. In our model the nature of the seismic Moho varies on a segment scale, according to the different tectonic features that characterize the studied segments.

The *PmP* reflector observed at the center of OH-1 probably corresponds to the base of a Moho transition zone. Within this transition zone, numerous gabbro sills may be accumulated in the top, and their relative volume with respect to the surrounding dunites may progressively decrease with depth. The level at which a permeability barrier may control the formation of gabbro sills [*Kelemen and Aharonov*, 1998] may be associated with the seismic Moho. This petrological Moho may be present also at the outside corners of OH-1 and OH-2 and the center of OH-2, although it is probably associated with a much thinner transition zone. The seismic Moho beneath the inside corners of OH-1 and OH-2 likely represents a serpentinization front. We prefer this interpretation on the basis of the gravity data, which require that serpentinites at NTO-1 extend toward the inside corners. We have not found a seismic Moho at the NTO-1. The lack of *PmP* reflection from any boundary at the NTO-1 and the absence of any first-order velocity discontinuities in the model suggest, at this section of the profile, that fracturing and serpentinization dominate the lithospheric structure in a way that does not require important velocity changes.

8. Conclusions

A schematic geological interpretation of our results is presented in Figure 13. The summarized conclusions of this study are as follows:

1. The structure at the center of segment OH-1 is characterized by a Moho transition zone which is thick (~2.5 km) at the midpoint and thins away from it. The anomalous seismic velocities within this layer (7.2-7.6 km/s) suggest that it could be composed of 70-80% of igneous gabbro sills alternating with dunites. The igneous crustal thickness at the center of this segment is 8.1-8.3 km. In contrast, the Moho at the center OH-2 corresponds to a first-order velocity discontinuity, yielding a crustal thickness of 6.6±0.3 km.

2. Segments OH-1 and OH-2 have similar average crustal thicknesses (6.0±1.2 km and 6.1±0.7 km, respectively) and thus a similar overall magma supply. The differences in axial morphology and gravity signature between these segments are a consequence of much larger along-axis crustal thickness variations at OH-1. This may reflect a more focused supply of melt from the mantle beneath OH-1 or less efficient along-axis magma transport at crustal levels, perhaps due to the proximity of OH-1 to the OFZ.

3. The seismic structure of a small nontransform offset is characterized by a continuous velocity gradient from low, extrusive velocities to ultramafic velocities. We interpret this structure as highly fractured and altered mafic crust (3.8 km maximum thickness) possibly disrupted by ultramafic outcrops, overlaying a partially serpentinized mantle with serpentinization of 40% at ~3.8 km below the seafloor and 10% at ~6.2 km.

4. There is a more rapid shoaling of the Moho from the segment centers to the inside corners than to the outside corners, suggesting that inside-corner crust of both segments has been tectonically thinned. No important differences are found in the depth to the Moho between inside and outside corners, probably because at the outside corners the Moho represents a lithological boundary, while at the inside corners it may represent a serpentinization front. Thus the igneous crust at the inside corners is thinner than at the outside corners.

5. The differences in the velocity structure between the inside and outside corners are more apparent at OH-2 than at OH-1.

The higher average velocity at the inside corner of OH-2 suggests that the axial extrusive layer is thinner at the northern end of OH-2 than at the southern end of OH-1 probably due to along-axis magma migration away from the injection zone and not due to magma supply differences.

6. The nature of the seismically defined Moho varies according to the relative importance of tectonic versus magmatic processes. The seismic Moho is attributed to the base of a thick transition zone at OH-1, where magma supply is highly focused, to a pure mafic-to-ultramafic contact at the outside corners and segment center of OH-2 and to a serpentinization front at the inside corner and segment discontinuities.

Aknowledgments. We thank Captain Ian Young, Science Officer Joe Stennett, and the crew of the R/V *Maurice Ewing* Leg 96-08 for the data acquisition. We are grateful to the WHOI OBS group, namely, John Bailey, Jim Dolan, Dave DuBois, John Hallinan, and Beecher Wooding, for their technical support. This study benefited from discussions with and suggestions from Javier Escartín, Josep Gallart, Emilie Hooft, Allegra Hosford, and Graham Kent. We also thank JGR reviewers Tim Minshull and John Osler and Associate Editor Keith Louden for their helpful suggestions and constructive criticism. The GMT software package [*Wessel and Smith*, 1995] was used in the preparation of this paper. J. Escartín kindly provided the location of the Atlantic fracture zones presented in Figure 2a. This work was supported by the National Science Foundation grant OCE-93-00450 to the Woods Hole Oceanographic Institution. J.P.C. was supported by a Ministerio de Educación y Ciencia (Spain)/Fulbright Postdoctoral Fellowship (FU96-28992999). Woods Hole Oceanographic Institution contribution 10088.

References

Barclay, A.H., D.R. Toomey, and S.C. Solomon, Seismic structure and crustal magmatism at the Mid-Atlantic Ridge, 35°N, *J. Geophys. Res., 103*, 17,827-17,844, 1998.

Bideau, D., R. Hekinian, C. Bollinger, M. Constantin, E. Gràcia, C. Guivel, B. Sichler, R. Apprioual, and R. Le Gall, Submersible investigations of highly contrasted magmatic activities recorded on two segments of the Mid-Atlantic Ridge near 34°52'N and 33°55'N, *InterRidge News, 5*(1), 9-14, 1996.

Birch, F., The velocity of compressional waves in rocks to 10 kilobars, *J. Geophys. Res., 65*, 1083-1102, 1960.

Blackman, D.K., and D.W. Forsyth, Isostatic compensation of tectonic features of the Mid-Atlantic Ridge: 25°-27°30'S, *J. Geophys. Res., 96*, 11,741-11,758, 1991.

Blackman, D.K., J.R. Cann, B. Janssen, and D.K. Smith, Origin of extensional core complexes: evidences from the Mid-Atlantic Ridge at Atlantis fracture zone, *J. Geophys. Res., 103*, 21,315-21,333, 1998.

Cannat, M., C. Mével, M. Maia, C. Deplus, C. Durand, P. Gente, P. Agrinier, A. Belarouchi, G. Dubuisson, E. Humler, and J. Reynolds, Thin crust, ultramafic exposures, and rugged faulting patterns at the Mid-Atlantic Ridge (22°-24°N), *Geology, 23*, 49-52, 1995.

Carlson, R.L., and G.S. Raskin, Density of the ocean crust, *Nature, 311*, 555-558, 1984.

Christensen, N.I., Elasticity of ultrabasic rocks, *J. Geophys. Res., 71*, 5921-5931, 1966.

Christensen, N.I., The magnitude, symmetry and origin of upper mantle anisotropy based on fabric analyses of ultramafic tectonites, *Geophys. J. R. Astron. Soc., 76*, 89-111, 1984.

Christensen, N.I., and J.D. Smewing, Geology and seismic structure of the northern section of the Oman ophiolite, *J. Geophys. Res., 86*, 2545-2555, 1981.

Coleman, R.G., Petrological and geophysical nature of serpentinites, *Geol. Soc. Am. Bull., 82*, 897-918, 1971.

Collins, J.A., T.M. Brocher, and J.A. Karson, Two dimensional seismic reflection modeling of the inferred fossil oceanic crust/mantle transition in the Bay of Islands ophiolite, *J. Geophys. Res., 91*, 12,520-12,538, 1986.

Creager, K.C., and L.M. Dorman, Location of instruments on the seafloor by joint adjustment of instrument and ship position, *J. Geophys. Res., 87*, 8379-8388, 1982.

DeMets, C., R.G. Gordon, D.F. Argus, and S. Stein, Current plate motions, *Geophys. J. Int., 101*, 425-478, 1990.

Deplus, C., J. Escartín, A. Briais, M. Cannat, J. Georgen, J. Lin, S. Mercouriev, C. Meyzen, M. Muller, G. Pouliquen, A. Rabain, and P. da Silva, Linking variation in magma supply and segment growth: Temporal evolution of segment OH-1 (MAR at 35°N) during the last 12 Myr, *Eos Trans. AGU, 79*(45), Fall Meet. Suppl., F856, 1998.

Detrick, R.S., and G.M. Purdy, The crustal structure of the Kane fracture zone from seismic refraction studies, *J. Geophys. Res., 85*, 3759-3778, 1980.

Detrick. R.S., R.S. White, and G.M. Purdy, Crustal structure of North Atlantic fracture zones, *Rev. Geophys., 31*, 439-458, 1993.

Detrick, R.S., H.D. Needham, and V. Renard, Gravity anomalies and crustal thickness variations along the Mid-Atlantic Ridge between 33°N and 40°N, *J. Geophys. Res., 100*, 3767-3787, 1995.

Detrick, R.S., J.A. Collins, G.M. Kent, J. Lin, and D.R. Toomey, Mid-Atlantic Ridge Bullseye seismic refraction and multichannel reflection experiment, R/V *Maurice Ewing Leg 96-08, Cruise Rep.*, 120 pp., Woods Hole Oceanogr. Inst., Woods Hole, Mass., 1996.

Dick, H.J.B., W.B. Bryan, and G. Thompson, Low-angle faulting and steady-state emplacement of plutonic rocks at ridge-transform intersections, *Eos Trans. AGU, 62*, 406, 1981.

Dick, H.J.B., P.S. Meyer, S. Bloomer, S. Kirby, D.S. Stakes, and C. Mawer, Lithostratigraphic evolution of an in situ section of oceanic layer 3, *Proc. Ocean Drill. Program Sci. Results, 118*, 439-538, 1991.

Escartín, J., and J. Lin, Ridge offsets, normal faulting, and gravity anomalies of slow spreading ridges, *J. Geophys. Res., 100*, 6163-6177, 1995.

Escartín, J., and J. Lin, Tectonic modification of axial crustal structure: Evidence from spectral analyses of residual gravity and bathymetry of the Mid-Atlantic Ridge flanks, *Earth Planet. Sci. Lett., 154*, 279-293, 1998.

Fialko, Y.A., and A.M. Rubin, Thermodynamics of lateral dike propagation: Implications for crustal accretion at slow spreading mid-ocean ridges, *J. Geophys. Res., 103*, 2501-2514, 1998.

Goff, J.A., B.E. Tucholke, J. Lin, G. Jaroslow, and M.C. Kleinrock, Quantitative analysis of abyssal hills in the Atlantic Ocean: A correlation between inferred crustal thickness and extensional faulting, *J. Geophys. Res., 100,* 22,509-22,522, 1995.

Gràcia, E., D. Bideau, R. Hekinian, Y. Lagabrielle, and L.M. Parson, Along-axis magmatic oscillations and exposures of ultramafics rocks in a second-order segment of the Mid-Atlantic Ridge (33°43'N to 34°07'N), *Geology, 25*, 1059-1062, 1997.

Henstock, T.J., R.S. White, and J.H. McBride, Along-axis variability in crustal accretion at the Mid-Atlantic Ridge: results from the OCEAN study, *J. Geophys. Res., 101*, 13,673-13,688, 1996.

Holbrook, W.S., E.C. Reiter, G.M. Purdy, D. Sawyer, P.L. Stoffa, J.A. Austin Jr., J. Oh, and J. Makris, Deep structure of the U.S. Atlantic continental margin, offshore South Carolina, from coincident ocean bottom and multichannel seismic data, *J. Geophys. Res., 99*, 9155-9178, 1994.

Hooft, E.E.E., R.S. Detrick, D.R. Toomey, J.A. Collins, and J. Lin, Crustal and upper mantle structure along three contrasting spreading segments of the Mid-Atlantic Ridge, 33.5°-35°N, *J. Geophys. Res.*, in press, 1999.

Horen, H., M. Zamora, and G. Dubuisson, Seismic waves velocities and anisotropy in serpentinized peridotites from Xigaze ophiolite: Abundance of serpentinite in slow spreading ridge, *Geophys. Res. Lett., 23*, 9-12, 1996.

Hosford, A., R.S. Detrick, J.A. Collins, J. Lin, and D.R. Toomey, Seismic structure and gravity models of inside-corner crust at 35°N on the Mid-Atlantic Ridge, *Eos Trans. AGU, 79*(17), Spring Meet. Suppl., S335, 1998.

Karson, J.A., and H.J.B. Dick, Tectonics of ridge-transform intersection at the Kane Fracture Zone, *Mar. Geophys. Res., 6*, 51-98, 1983.

Karson, J.A., J.A. Collins, and J.F. Casey, Geologic and seismic velocity structure of the crust/mantle transition in the Bay of Islands ophiolite complex, *J. Geophys. Res., 89*, 6126-6138, 1984.

Kelemen, P.B., and E. Aharonov, Periodic formation of magma fractures and generation of layered gabbros in the lower crust beneath oceanic spreading ridges, in *Faulting and Magmatism at Mid-Ocean Ridges, Geophys. Monogr. Ser.,* vol. 106, edited by W.R. Buck et al., pp. 267-289, AGU, Washington, D.C., 1998.

Kelemen, P.B., and W.S. Holbrook, Origin of thick, high-velocity igneous crust along the U.S. East Coast Margin, *J. Geophys. Res., 100*, 10,077-10,094, 1995.

Kelemen, P.B., N. Shimizu, and V.J.M. Salters, Extraction of mid-ocean ridge basalt from the upwelling mantle by focused flow of melt in dunite channels, *Nature, 375*, 747-753, 1995.

Kelemen, P.B., K. Koga, and N. Shimizu, Geochemistry of gabbro sills in the crust-mantle transition zone of the Oman ophiolite: Implications for the origin of the oceanic lower crust, *Earth Planet. Sci. Lett., 146*, 475-488, 1997.

Korenaga, J., and P.B. Kelemen, Origin of gabbro sills in the Moho transition zone of the Oman ophiolite: Implications for magma transport in the oceanic lower crust, *J. Geophys. Res., 102*, 27,729-27,749, 1997.

Kuo, B.-Y., and D.W. Forsyth, Gravity anomalies of the ridge-transform system in the South Atlantic between 31° and 34.5°S: Upwelling centers and variations in crustal thickness, *Mar. Geophys. Res., 10*, 205-232, 1988.

LeDouaran, S., H.D. Needham, and J. Francheteau, Pattern of opening rates along the axis of the Mid-Atlantic Ridge, *Nature, 300*, 254-257, 1982.

Lin, J., G.M. Purdy, H. Schouten, J.-C. Sempéré, and C. Zervas, Evidence from gravity data for focused magmatic accretion along the Mid-Atlantic Ridge, *Nature, 344*, 627-632, 1990.

Macdonald, A.H., and W.S. Fyfe, Rate of serpentinization in seafloor environments, *Tectonophysics, 116*, 123-135, 1985.

Macdonald, K.C., The crest of the Mid-Atlantic Ridge: Models for crustal generation processes and tectonics, in *The Geology of North America, The Western North Atlantic Region,* vol. M, edited by P.R. Vogt and B.E. Tucholke, pp. 51-68, Geol. Soc. of Am., Boulder, Colo., 1986.

Magde, L.S., A.H. Barclay, D.R. Toomey, R.S. Detrick, and J.A. Collins, Crustal magma plumbing within a segment of the Mid-Atlantic Ridge, 35°N, *Earth Planet. Sci. Lett.*, in press, 1999.

McKenzie, D., and M.J. Bickle, The volume and composition of melt generated by extension of the lithosphere, *J. Petrol., 29*, 625-679, 1988.

Mével, C., M. Cannat, P. Gente, E. Marion, J.M. Auzende, and J.A. Karson, Emplacement of deep crustal and mantle rocks on the west median valley wall of the MARK area (MAR, 23°N), *Tectonophysics, 190*, 31-53, 1991.

Miller, D.J., and N.I. Christensen, Seismic velocities of lower crustal and upper mantle rocks from the slow spreading Mid-Atlantic Ridge, south of the Kane transform zone (MARK), in *Proc. Ocean Drill. Program Sci. Results, 153*, 437-454, 1997.

Minshull, T.A., R.S. White, J.C. Mutter, P. Buhl, R.S. Detrick, C.A. Williams, and E. Morris, Crustal structure at the Blake Spur fracture zone from expanding spread profiles, *J. Geophys. Res., 96*, 9955-9984, 1991.

Muller, M.R., C.J. Robinson, T.A. Minshull, R.S. White, and M.J. Bickle, Thin crust beneath ocean drilling program borehole 735B at the Southwest Indian Ridge?, *Earth Planet. Sci. Lett., 148*, 93-107, 1997.

Nicolas, A., and F. Boudier, Mapping oceanic ridge segments in Oman ophiolite, *J. Geophys. Res., 100*, 6179-6197, 1995.

O'Hanley, D.S., *Serpentinites: Records of Tectonic and Petrological History, Oxford Monogr. Geol. Geophys.,* vol. 34, 277 pp., Oxford Univ. Press, New York, 1996.

Parker, R.L., The rapid calculation of potential anomalies, *Geophys. J. R. Astron. Soc., 31*, 447-455, 1972.

Phipps Morgan, J., and D.W. Forsyth, Three-dimensional flow and temperature perturbations due to a transform offset: Effects on oceanic crustal and upper mantle structure, *J. Geophys. Res., 93*, 2955-2966, 1988.

Schouten, H., K.D. Klitgord, and J.A. Whitehead, Segmentation of mid-ocean ridges, *Nature, 317*, 225-229, 1985.

Sempéré, J.-C., J. Lin, H.S. Brown, H. Schouten, and G.M. Purdy, Segmentation and morpho-tectonic variations along a slow-spreading center: The Mid-Atlantic Ridge (24°N-30°40'N), *Mar. Geophys. Res., 15*, 153-200, 1993.

Severinghaus, J.P., and K.C. Macdonald, High inside corners at ridge-transform intersections, *Mar. Geophys. Res., 9*, 353-367, 1988.

Shaw, P.R., Ridge segmentation, faulting and crustal thickness in the Atlantic Ocean, *Nature, 358*, 490-493, 1992.

Shaw, W.J., and J. Lin, Causes and consequences of variations in faulting style at the Mid-Atlantic Ridge, *J. Geophys. Res., 98*, 21,839-21,851, 1993.

Sinha, M.C., and K.E. Louden, The Oceanographer fracture zone, I, Crustal structure from seismic refraction studies, *Geophys. J. R. Astron. Soc., 75*, 713-736, 1983.

Sleep, N.H., Formation of oceanic crust: Some thermal constraints*, J. Geophys. Res., 80*, 4037-4042, 1975.

Smith, D.K., and J.R. Cann, The role of seamount volcanism in crustal construction at the Mid-Atlantic Ridge (24°-30°N), *J. Geophys. Res., 97*, 1645-1658, 1992.

Takahashi, N., Evidence for melt segregation towards fractures in the Horoman mantle peridotite complex, *Nature*, 359, 52-55, 1992.

Thibaud, R., P. Gente, and M. Maia, A systematic analysis of the Mid-Atlantic Ridge morphology and gravity between 15°N and 40°N: Constraints of the thermal structure, *J. Geophys. Res., 103*, 24,223-24,243, 1998.

Tivey, M.A., and B.E. Tucholke, Magnetization of 0-29 Ma ocean crust on the Mid-Atlantic Ridge, 25°30' to 27°10'N, *J. Geophys. Res., 103*, 17,807-17,826, 1998.

Toomey, D.R., S.C. Solomon, and G.M. Purdy, Tomographic imaging of the shallow crustal structure of the East Pacific Rise at 9°30'N, *J. Geophys. Res., 99*, 24,135-24,157, 1994.

Tucholke, B.E., and J. Lin, A geological model for the structure of ridge segments in slow spreading ocean crust, *J. Geophys. Res., 99*, 11,937-11,958, 1994.

Wessel, P., and W.H.F. Smith, New version of the generic mapping tools released, *Eos Trans. AGU, 76*, 329, 1995.

White, R.S., R.S. Detrick, M.C. Sinha, and M.-H. Cormier, Anomalous seismic crustal structure of oceanic fracture zones, *Geophys. J. R. Astron. Soc., 79*, 779-798, 1984.

White, R.S., D. McKenzie, and R.K. O'Nions, Oceanic crustal thickness from seismic measurements and rare earth element inversions, *J. Geophys. Res., 97*, 19,683-19,715, 1992.

Zelt, C.A., and R.B. Smith, Seismic traveltime inversion for 2-D crustal velocity structure, *Geophys. J. Int., 108*, 16-34, 1992.

J.P Canales, J.A. Collins, R.S. Detrick, and J. Lin, Department of Geology and Geophysics, Woods Hole Oceanographic Institution, 360 Woods Hole Road, Woods Hole, MA 02543. (jpcanales@whoi.edu; jcollins@whoi.edu rdetrick@whoi.edu; jlin@whoi.edu)

D.R. Toomey, Department of Geological Sciences, University of Oregon, 1272 Geological Sciences, Eugene, OR 97403-1272. (drt@newberry.uoregon.edu)

(Received January 20, 1999; revised July 6, 1999;
accepted October 21, 1999.)